

¹ Hourly Assimilation of Different Sources of Observations Including
² Satellite Radiances in a Mesoscale Convective System Case During
³ RELAMPAGO campaign

⁴ Paola Belén Corrales^{a,b,c,1}, V. Galligani^{a,b,c}, Juan Ruiz^{a,b,c}, Luiz Sapucci^f, María Eugenia
⁵ Dillon^{d,e}, Yanina García Skabar^{d,e,c}, Maximiliano Sacco^d, Craig S. Schwartz^g, Stephen W.
⁶ Nesbitt^h

^a*Universidad de Buenos Aires Facultad de Ciencias Exactas y Naturales Departamento de Ciencias de la Atmosfera y los Oceanos. Buenos Aires Argentina.*

^b*CONICET – Universidad de Buenos Aires. Centro de Investigaciones del Mar y la Atmosfera (CIMA). Buenos Aires Argentina.*

^c*CNRS – IRD – CONICET – UBA. Instituto Franco-Argentino para el Estudio del Clima y sus Impactos (IRL 3351 IFAECI). Buenos Aires Argentina.*

^d*Servicio Meteorológico Nacional de Argentina.*

^e*CONICET (Consejo Nacional de Investigaciones Científicas y Técnicas).*

^f*National Institute for Space Research Brazil Center for Weather Forecasting and Climate Studies.*

^g*National Center for Atmospheric Research Boulder Colorado.*

^h*Department of Atmospheric Sciences University of Illinois Urbana-Champaign Urbana Illinois.*

⁷ **Abstract**

This paper evaluates the impact of assimilating high-resolution surface networks and satellite observations using the WRF-GSI-LETKF over central and north eastern Argentina where the surface and upper air observing networks are relatively coarse. A case study corresponding to a huge mesoscale convective system (MCS) that developed during November 22, 2018 was used. The accumulated precipitation associated with this MCS was quite high, exceeding 200 mm over northern Argentina and Paraguay. The MCS developed during the Intense Observing Period (IOP) of the Remote sensing of Electrification, Lightning, And Mesoscale/microscale Processes with Adaptive Ground Observations (RELAMPAGO) field campaign. The GSI-4DLETKF data assimilation package is used to produce analyses by assimilating observations every hour with 10-km horizontal grid spacing and a 60-member multiphysics ensemble. Four assimilation experiments are conducted using different sets of observations: CONV, consisting of conventional observations from NCEP's prepBUFR files; AWS, combining CONV and dense automatic surface weather station networks (AWS),

SATWND, combining AWS with satellite-derived winds, and RAD, including SATWND; and satellite radiances from different microwave and infrared sensors. The assimilation of observations with high temporal and spatial frequency generates an important impact on the PBL, primarily on the precipitable water content, that leads to the development of deep convection and heavy precipitation closer to the observed in this case study. The assimilation of radiance observations produces a better development of the convection mainly during the mature state of the MCS leading to an increase in the accumulated precipitation. Ensemble forecasts initialized from each experiment were also simulated to evaluate their skill to predict precipitation. The hourly assimilation of the observations in AWS, SATWND, and RAD helped to improve the precipitation forecast.

8 *Keywords:* Regional Data Assimilation, Surface Observations, Satellite Observations,

9 Regional Data Assimilation, Surface Observations, Satellite Observations

10 **1. Introduction**

11 Severe weather events cause significant human and economic losses around the world. A
12 large number of these phenomena are associated with the occurrence of deep moist convec-
13 tion, including tornadoes, intense wind gusts, extreme precipitation in short time periods,
14 large hail, and lightning. Southern South America has one of the highest frequencies in the
15 world of favorable conditions for high-impact meteorological events (Brooks et al., 2003)
16 and large hail events (Cecil and Blankenship, 2012), particularly during austral spring and
17 summer. This is also confirmed by observational evidence and high impact weather reports
18 (Matsudo et al., 2015; Rasmussen et al., 2014). Recently, the Remote sensing of Electrifica-
19 tion, Lightning, And Mesoscale/microscale Processes with Adaptive Ground Observations
20 (RELAMPAGO) field campaign (Nesbitt et al., 2021) has been conducted to investigate
21 the mechanisms for convective initiation and the occurrence of high-impact weather events
22 associated with deep convection in central Argentina.

*Corresponding author

Email address: paola.corrales@cima.fcen.uba.ar (Paola Belén Corrales)

¹Corresponding Author

23 Forecasting mesoscale meteorological phenomena and particularly deep moist convection
24 is a scientific and technological challenge due to its limited predictability and the difficulties
25 in diagnosing the state of the atmosphere at small spatial and short temporal scales (for
26 example from 1 to 10 kilometers and on the order of minutes). Mesoscale data assimilation
27 (DA) is an approach that can provide appropriate initial conditions for high-resolution nu-
28 mercial forecasts (Sun et al., 2014) and thus has received increasing attention in the last
29 decades.

30 For DA methods to be successful, observing networks with sufficient temporal and spa-
31 tial resolution capable of capturing mesoscale variability should be used (Gustafsson et al.,
32 2018). Assimilating information on temperature, moisture, and wind in the planetary bound-
33 ary layer (PBL) improves mesoscale model initialization, and several authors have reported
34 the resultant beneficial impacts on the PBL structure and the location and timing of pre-
35 cipitating systems (e.g. Wheatley and Stensrud (2010), Ha and Snyder (2014), Chang et al.
36 (2017), Bae and Min (2022), Banos et al. (2021), Maejima et al. (2019), and Chen et al.
37 (2016)).

38 Particularly relevant for regional mesoscale DA systems in the region of interest is
39 that South America is characterized by a limited number of conventional observations
40 (i.e., radiosondes, surface weather stations) and operational networks that are not dense
41 enough to capture mesoscale details. In this context, analyzing the potential impact of non-
42 conventional sources of observations is essential to improve mesoscale numerical weather
43 prediction (NWP) over South America using DA. There have been only a few published
44 efforts on regional mesoscale DA, but they have all shown promising results (e.g. Dillon
45 et al., 2016, 2021; Goncalves de Goncalves et al., 2015). In particular, Dillon et al. (2021)
46 assimilated high resolution surface weather station networks, GOES-16 atmospheric motion
47 vectors (AMVs), and satellite temperature and moisture retrievals over central Argentina
48 with positive impacts. Similar to Gasperoni et al. (2018), Dillon et al. (2021) included private
49 weather station networks which are not incorporated in the operational analysis. However,
50 the impact of different observation types on the analysis quality has not been addressed.

51 The impact of non-conventional high spatial and temporal resolution observations, such

as AMVs, has been investigated in the context of regional mesoscale DA. Many studies have focused on the impact of these observations on the prediction of tropical storms (e.g., Wu et al. (2014), Cherubini et al. (2006), and Sawada et al. (2019), and many others). Most of these studies reported an overall positive impact of the assimilation of AMVs for this type of storm. However, some works indicated mixed impacts (e.g. Sawada et al. (2019) reported an improvement in the forecast of the track of the storm but a degradation in the forecast intensity). As stated in Zhao et al. (2021a,b), the impact of assimilating these data on high impact weather events associated with mid-latitude deep convection over land has received relatively less attention. Zhao et al. (2021a,b) assimilated GOES-16 AMVs into a storm-scale three-dimensional variational DA system during three high impact weather events. They reported positive impacts of AMVs on the characterization of the storm environment and improved short range precipitation forecasts. Otsuka et al. (2015) and Mallick and Jones (2020) found a slight improvement in the short-range precipitation forecast due to the storm-scale assimilation of high frequency AMVs.

While the assimilation of radiance observations into global models is well established (Eyre et al., 2020), the direct assimilation of radiance data into regional models, however, still remains a challenge due to the sparse data coverage (in the case of polar-orbiting satellite observations), bias correction, and the relatively low model tops used for this application. Bao et al. (2015) studied the impact of assimilating cloud-cleared microwave and infrared radiance data polar orbiting instruments on temperature and humidity forecasts over the western USA and found a reduction in the temperature bias at low and mid-levels as a result of the microwave observations but an opposite effect for infrared data. More recently, Zhu et al. (2019) studied the impact of assimilating clear sky polar orbiting satellite radiance data within a frequently updated regional system and showed an improvement for all variables, in particular for relative humidity at upper levels. Wang and Randriamampianina (2021) studied the impact of assimilating clear sky radiances in the high-resolution Copernicus European Regional Reanalysis. They reported that satellite radiance observations had a neutral impact on the analyses of geopotential height in the lower troposphere, while a slightly negative impact on the upper troposphere and the stratosphere. They also observed

81 similar results for 3-h forecasts initialized from the analysis but a positive impact on 12
82 and 24 -h forecasts. Given these mixed results, there is still room to analyze the utility of
83 assimilating radiance observations in a limited-area DA system over land. Moreover, to the
84 best of our knowledge, there are no studies related to the direct assimilation of radiance
85 observations over South America.

86 The main objective of this work is thus to contribute to the quantification and comparison
87 of the impact of high resolution automatic weather stations, AMVs, and clear-sky satellite
88 radiances, into a mesoscale, frequently-updated ensemble-based regional DA system. This
89 is particularly important in the efforts to improve mesoscale numerical weather prediction
90 (NWP) over South America where the conventional observation network is rather sparse
91 and other sources of information could potentially fill certain gaps. In particular, this paper
92 focuses on the impact in the context of a mid-latitude mesoscale convective system. To
93 reach this goal, several DA experiments are conducted for a case study of a large Mesoscale
94 Convective System (MCS) that developed over Southern South America during Nov 22-23,
95 2018 during the intense observation period (IOP) of the RELAMPAGO field campaign.

96 The paper is organized as follows. The DA system, the experimental design, and the
97 observations used are presented in section 2. Results are discussed in section 3 and finally,
98 conclusions are summarized in section 4.

99 **2. Data and Methods**

100 *2.1. Case overview*

101 Previously to the development of this case study, the center and north of Argentina was
102 immersed in a warm and humid air mass with high values of convective available potential
103 energy (CAPE), as shown by ERA 5 Reanalysis (Hersbach et al., 2018) in Figure 1a. On
104 Nov 22, 2018 a cold front crossed the center of Argentina (Figure 1b). This cold front
105 triggered isolated convective cells that rapidly grew upscale into an exceptionally large MCS
106 (Figure 1d,e). During that day several surface stations reported lightning, strong wind gusts,
107 and heavy rain. To the north of the region, a warm and humid environment contributed

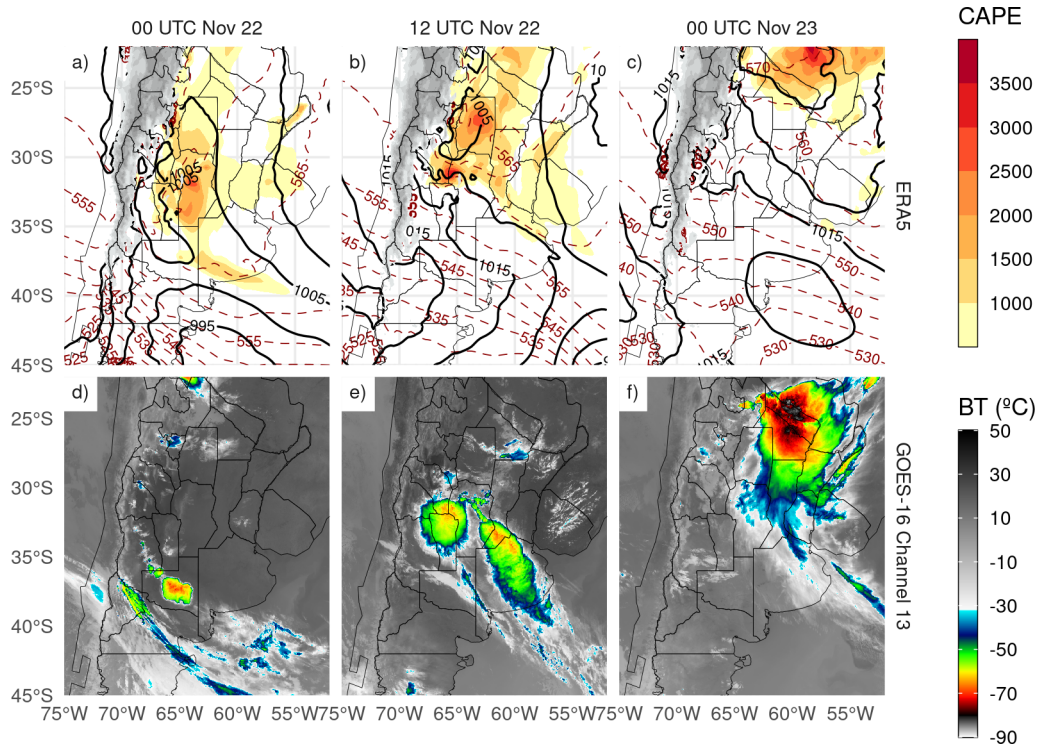


Figure 1: ERA5 Reanalysis of sea level pressure (hPa, black contours), 1000-500 hPa thickness (red dashed contours) and convective available potential energy (shaded) and GOES-16 channel 13 brightness temperature for a,d) 00 and b,e) 12 UTC Nov 22 and c,f) 00 UTC Nov 23.

108 to the development of isolated convection that ultimately grew and merged with the MCS
 109 (Figure 1f). The MCS traveled approximately 2500 km from south to north, dissipating
 110 over Paraguay and Southern Brazil after 42 hours.

111 2.2. Data assimilation system configuration

112 The forecast model uses the non-hydrostatic Advanced Research version of Weather Re-
 113 search and Forecasting (WRF-ARW V3.9.1, Skamarock et al. (2008)). The horizontal grid
 114 spacing is 10 km (150 x 200 grid points) in the horizontal and 37 levels in the vertical with
 115 the top of the model at 50 hPa. The initial and boundary conditions are provided by the
 116 Global Forecast System (GFS) analysis (0.25° horizontal grid spacing and 6-hour tempo-
 117 ral resolution; National Centers for Environmental Prediction, National Weather Service,
 118 NOAA, U.S. Department of Commerce (2015)). In this case, a single nesting approach is

119 used since the resolution gap between the driving model and the regional model is not too
120 large (0.25° or 25 km approximately to 10 km). This approach is also based on recent stud-
121 ies which suggest that using multiple nested domains does not necessarily lead to improved
122 precipitation forecasts in regional domains, particularly in areas of complex terrain (e.g.
123 Liang et al. (2019), Beck et al. (2004)). The domain covers the area indicated in Figure 2
124 to capture the development of the MCS during the simulated period.

125 The analyses are generated using the LETKF implementation (V1.3, Hunt et al. (2007))
126 of the Gridpoint Statistical Interpolation analysis system (GSI V3.8; Shao et al. (2016)). A
127 rapid update cycle approach is implemented with hourly analysis and a centered assimila-
128 tion window, meaning that all the observations within ± 30 minutes of the analysis time
129 are assimilated. Observations are assimilated in a 4D approach by comparing them with
130 the corresponding first guess state at 10-minute intervals. For radiance observations, the
131 Community Radiative Transfer Model version 2.3 (CRTM; Han et al. (2006)) is used as an
132 observation operator to calculate model-simulated brightness temperatures.

133 A 60-member ensemble is used where the initial ensemble mean and the mean boundary
134 conditions are taken from the GFS deterministic analysis. A set of 60 perturbations are
135 randomly generated to perturb the initial state as well as the boundary conditions during the
136 length of the experiment. Perturbing the boundary conditions helps to reduce the impact of
137 errors in the driving global model and helps to keep a larger ensemble spread throughout the
138 domain and during the length of the experiment (Ouaraini et al., 2015). The perturbations
139 are generated as scaled differences between two random atmospheric states obtained from
140 the Climate Forecast System Reanalysis (CFSR) data with 0.5° horizontal grid spacing with
141 a smooth time evolution as in Necker et al. (2020) and Maldonado et al. (2021). In this way,
142 the nearly hydrostatic and geostrophic equilibrium of larger scales is preserved. The random
143 perturbations used are the same across experiments to ensure that the differences between
144 experiments are only related to changes in the number and type of assimilated observations.

145 A multi-physics scheme is used to better represent the uncertainty in the model formula-
146 tion within the DA system. 9 different model configurations are generated consisting of the
147 combination of 3 moist convection schemes (Kain–Fritsch (Kain, 2004), Grell–Freitas (Grell

Table 1: Generation of the 60-member multi-physics ensemble as a combination of Cumulus and PBL parameterizations.

Cumulus	PBL		
	MYJ	MYNN2	YSU
BMJ	5, 14, 23, 32, 41, 50, 59	8, 17, 26, 35, 44, 53	2, 11, 20, 29, 38, 47, 56
GF	6, 15, 24, 33, 42, 51, 60	9, 18, 27, 36, 45, 54	3, 12, 21, 30, 39, 48, 57
KF	4, 13, 22, 31, 40, 49, 58	7, 16, 25, 34, 43, 52	1, 10, 19, 28, 37, 46, 55

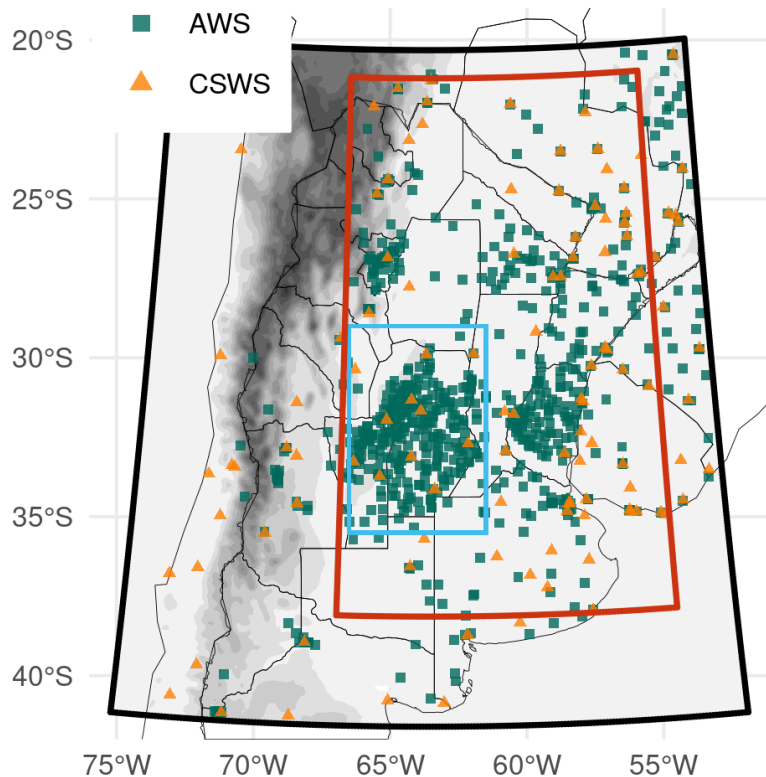
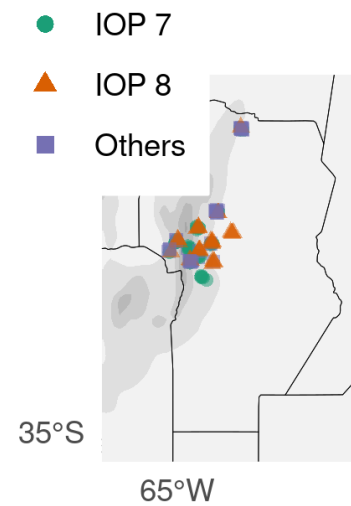
and Freitas, 2013), and Betts–Miller–Janjic (Janjić, 1994)) and 3 planetary boundary layer schemes (Yonsei University Scheme (Hong et al., 2006b), Mellor–Yamada–Janjic Scheme (Janjić, 1994), and Mellor–Yamada Nakanishi Niino (Nakanishi and Niino, 2009)). The distribution of these schemes among the 60 ensemble members is outlined in Table 1. The multi-physics approach is also introduced in order to represent the uncertainty associated with the more relevant physical processes that are not resolved by the model. All ensemble members use the same land-surface model (Noah-MP, Chen and Dudhia (2001)), micro-physics (WRF single-moment 6-class scheme (Hong et al., 2006a)), and radiation processes (RRTMG shortwave and longwave scheme (Iacono et al., 2008)) parameterizations.

To reduce the effect of spurious correlations in the estimation of error covariances, a horizontal localization radius of 180 km and a vertical localization radius of 0.4 (in log pressure coordinates) is used as in Dillon et al. (2021) for all types of observations. A relaxation-to-prior spread inflation (Whitaker and Hamill, 2012) is applied with an inflation parameter $\alpha = 0.9$ following Maldonado et al. (2020) to mitigate the impact of sampling errors and to consider model errors not accounted for by the multi-model ensemble approach.

2.3. Observations

2.3.1. Conventional

The conventional observations used are part of the Global Data Assimilation System (GDAS) data stream. Conventional observations included in the Binary Universal Form for Representation of Meteorological Data (PREPBUFR) files generated at the National

a)**b)**

Altitude (m) 0 1000 2000 3000 4000 5000 6000

Figure 2: a) The domain used for the simulations (black box), the inner domain used for the experiment comparison (red box), the region shown in b) (light blue box), and the locations of Automatic Weather Stations (AWS, green squares) and Conventional Surface Weather Stations (CSWS, orange triangles). b) Locations of radiosonde launches during RELAMPAGO. Green dots correspond to radiosondes launched during IOP 7, orange triangles are radiosondes launched during IOP 8, and purple squares are radiosondes launched outside the IOP missions. The topography in meters is also shown (shaded).

168 Centers for Environmental Prediction (NCEP) are assimilated. These consist of surface
169 observations from 117 Conventional Surface Weather Stations (CSWS), ships, and upper-
170 air observations from 13 radiosondes sites and aircraft. The orange triangles in Figure 2a
171 indicate the location of the surface stations included in this experiment. The frequency of
172 these observations varied between 1 hour for surface stations and 12/24 hours for radiosondes.
173 Wind surface observations over oceans (ASCATW) come from scatterometers and are also
174 included in the PREPBUFR files.

175 Table 2 lists all the observation types (i.e., surface pressure, temperature, specific hu-
176 midity, and wind) available for each source, together with their associated errors. The
177 observation errors were specified following the GSI default configuration. In some cases,
178 the error varies with height and depends on the specific platform (aircraft and satellite-
179 derived wind). In terms of quality control, a gross check was performed by the observation
180 operator by comparing the innovation (the difference between the observation and the model-
181 simulated observation based on the first-guess) with a predefined threshold that depends on
182 the observation error (also included in Table 2).

183 *2.3.2. AWS networks*

184 Data from 866 Automatic Weather Stations (AWS) that are part of 17 public and private
185 surface networks over Southern South America are also assimilated. The dataset used in
186 this study has been obtained from the RELAMPAGO Data Set repository (Garcia et al.,
187 2019). These stations are indicated as green squares in Figure 2a. They have higher spatial
188 coverage than the CSWS and a sampling frequency of 10 minutes in most cases. All stations
189 measure temperature, but only 395 stations provide humidity, 422 provide pressure, and 605
190 provide wind information. Observation errors used to assimilate these observations are the
191 same as for the CSWS (see Table 2).

192 *2.3.3. Satellite-derived winds*

193 Satellite-derived wind observations are also included in the PREPBUFR files available
194 every 6 h, and consist of estimations from GOES-16 (using the visible, infrared, and water
195 vapor channels) and METEOSAT 8 and 11 (using the visible and water vapor channels).

Table 2: Characteristics of the assimilated observations: The code for each observation type and its source, the available variables, the observation error, and the gross check thresholds used.

Code	Platform	Variable	Error	Gross check
CSWS	Surface weather stations	Pressure	1-1.6 hPa*	3.6 hPa
		Temperature	1.5 K	7 K
		Specific humidity	20 %	8 gKg ⁻¹
		Wind	2.2 ms ⁻¹	6 ms ⁻¹
ADPUPA	Radiosondes	Pressure	1.1-1.2 hPa**	4 hPa
		Temperature	0.8-1.5 K*	8 K
		Specific humidity	20 %	8 gKg ⁻¹
		Wind	1.4-3 ms ⁻¹ *	8 ms ⁻¹
AIRCFT	Aircrafts	Temperature	1.47-2.5 K ⁺	7 K
		Wind	2.4-3.6 ms ⁻¹ ⁺	6.5-7.5 ms ⁻¹ ⁺
ASCATW	Advanced Scatterometers	Wind	1.5 ms ⁻¹	5 ms ⁻¹
SFCSHP	Ships and Buoys	Pressure	1.3 hPa	4 hPa
		Temperature	2.5 K	7 K
		Specific humidity	20 %	8 gKg ⁻¹
		Wind	2.5 ms ⁻¹	5 ms ⁻¹
SATWND	Satellite-derived winds	Wind	3.8-8 ms ⁻¹ ^{*,+}	1.3-2.5 ms ⁻¹ ⁺

* Observation error varied with height.

** Observations above 600 hPa are rejected.

+ Observation error depends on the report type.

196 Due to the domain covered by each of these satellites, GOES-16 is the primary source of
 197 satellite-derived winds (99 % of the observations). Observation errors used to assimilate
 198 these observations follow the GSI default configuration and are indicated in Table 2.

199 2.3.4. Satellite radiances

200 Satellite radiances available through the GDAS data stream, consisting of infrared and
 201 microwave observations, are used in this study. This includes the Advanced Microwave
 202 Sounding Unit - A (AMSU-A), Microwave Humidity Sounder (MHS), and 2 multispectral
 203 sensors; the Atmospheric Infrared Sounder (AIRS) and the Infrared Atmospheric Sounding

204 Interferometer (IASI) over several satellite platforms (see Table 3). Since the regional domain
 205 is located in the mid-latitudes and the satellite platforms of interest are on polar orbits, each
 206 sensor scans the area only twice a day with a spatial coverage depending on the satellite
 207 swath. For this reason, the number of satellite observations varied significantly among
 208 cycles. In particular, the multispectral sensors provided between 100 and 1000 observations
 209 for every scan every 12 hours, contributing 88 % of the total amount of assimilated radiances
 210 in our experiment. The vertical location of each radiance observation was estimated as the
 211 model level at which its weighting function was maximized as calculated by CRTM. The
 212 multispectral sensors have good vertical coverage and are able to sense from the lower
 213 troposphere up to the lower stratosphere.

214 The channels adopted for assimilation and their associated errors were defined taking
 215 into account the low model top (50 hPa). The data preprocessing, which is an essential
 216 step in the assimilation of radiances, was performed within the GSI system for each sensor
 217 specifically. First, a spatial data thinning is applied using a 60 km grid following Singh et al.
 218 (2016), Jones et al. (2013), and Lin et al. (2017), where the observations to be assimilated
 219 are chosen based on their distance to the model grid points, the observation quality (based
 220 on available data quality information), and the number of available channels (from the
 221 same pixel and sensor) that passed the quality control. Also, observations over the sea are
 222 preferred to those over land or snow (Hu et al., 2018).

223 The thinned observations were then bias corrected. The bias correction (BC) has an air-
 224 mass dependent and an angle-dependent component (Zhu et al., 2014) and it is calculated
 225 as a multi-linear function of N predictors $p_i(x)$, with associated coefficients β_i . Then, the
 226 bias corrected brightness temperature (BT_{bc}) can be obtained as:

$$BT_{bc} = BT + \sum_{i=0}^N \beta_i p_i(x) \quad (1)$$

227 GSI has a constant offset bias correction term ($p_0 = 1$) and the remaining predictors
 228 are the cloud liquid water content (CLW), the temperature lapse rate at the pressure of
 229 maximum weight, the square of the temperature lapse rate at the pressure of maximum

230 weight, and the emissivity sensitivity. Scan angle-dependent bias is modeled as a 4th-order
231 polynomial (Zhu et al., 2014).

232 In the GSI system, the β_i coefficients are trained using a variational estimation method
233 which solves the β_i that provides the best fit between the simulation and the observations.
234 The coefficients were initialized at 18 UTC Nov 18, 2018 with the GFS system coefficients.
235 The assimilation system was configured to use a constant background error variance of 0.01
236 to avoid large adjustments in the estimated coefficients at each time.

237 In our experiments, only clear-sky observations are used. For microwave radiances,
238 observations potentially contaminated by clouds are detected using the scattering and Liquid
239 Water Path (LWP) indexes (Weston et al., 2019; Zhu et al., 2016). For the infrared channels,
240 cloud contaminated observations are detected using the transmittance profile calculated
241 within the CRTM algorithms. Moreover, GSI checks the difference between the observations
242 and simulated brightness temperature with height to detect cloudy pixels. Additionally, the
243 GSI quality control for infrared sensors looks for observations over water with a large zenith
244 angle (over 60°) to reject channels near the visible range that can be contaminated with
245 reflection. It also performs an emissivity check for observations over land for both infrared
246 and microwave radiances.

247 2.3.5. Validation dataset

248 To evaluate the performance of the ensemble-based DA system presented in this article,
249 the following observational datasets were used:

- 250 • ERA5 hourly data on pressure levels from 1959 to present (Hersbach et al., 2018).
251 The variables of interest (air temperature, humidity and wind) were interpolated to
252 the model grid to compare them with the analysis of each experiment.
- 253 • The Multi-Network Composite Highest Resolution Radiosonde Data (UCAR/NCAR -
254 Earth Observing Laboratory, 2020) from the RELAMPAGO field campaign database
255 consisting of high-resolution radiosondes launched from several locations during the
256 IOPs along with the operational radiosondes. Only the soundings that did not enter

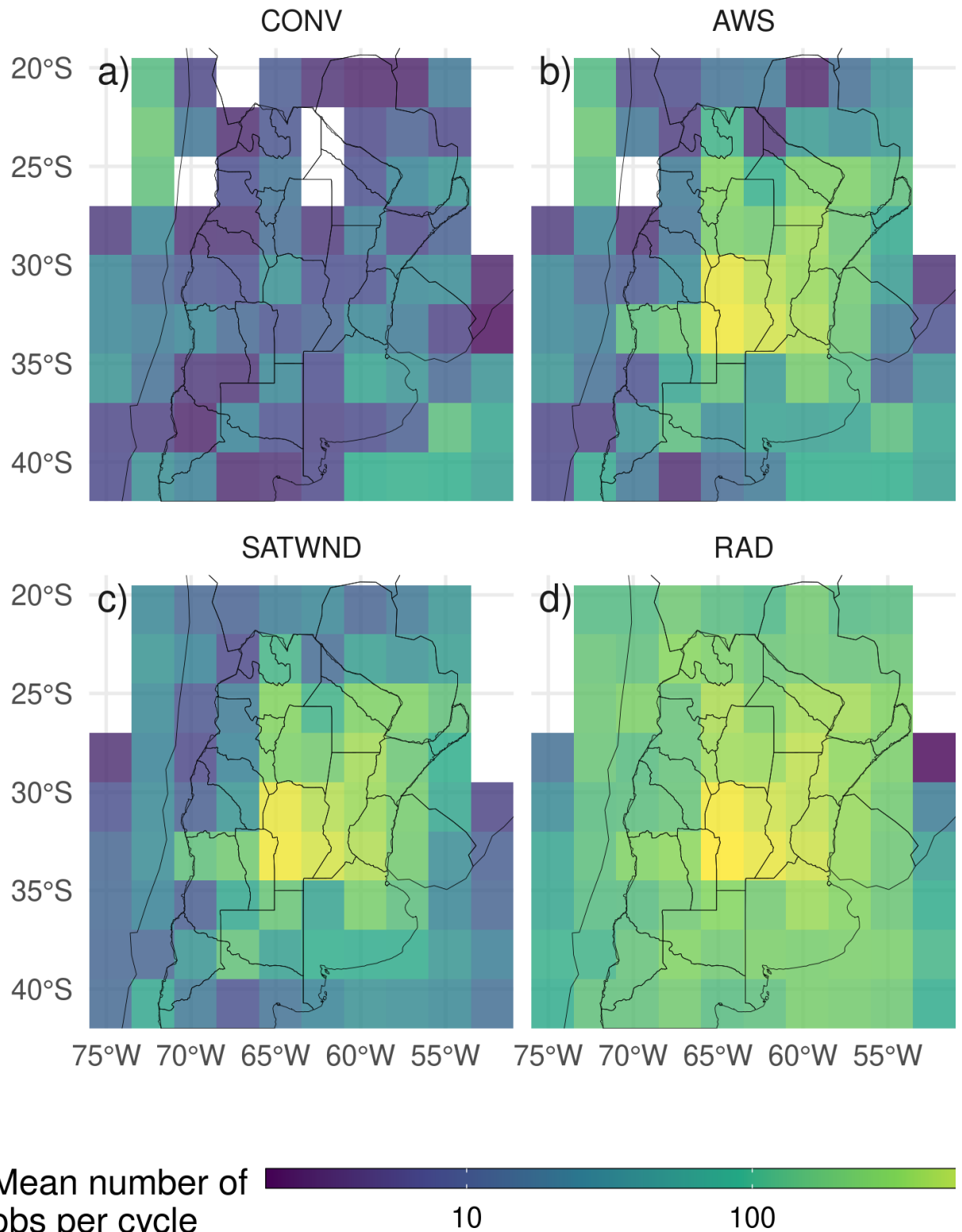


Figure 3: Horizontal spatial distribution of the mean available observations per analysis cycle for the a) CONV, b) AWS, c) SATWND, and d) RAD experiments calculated over 2.5° boxes.

Table 3: List of the available sensors over several platforms, the number of accepted channels for the assimilation, and the percentage of assimilated observations calculated over all radiance observations and all cycles.

Sensor	Platform	Assimilated channels	Percentage over total
AIRS	AQUA	52	31.63 %
AMSUA	NOAA15	2	3.31 %
	NOAA18	2	4.45 %
	METOP-A	2	2.08 %
IASI	METOP-A	66	52.72 %
	METOP-B	68	3.47 %
MHS	NOAA19	2	0.68 %
	METOP-A	3	0.8 %
	METOP-B	3	0.85 %

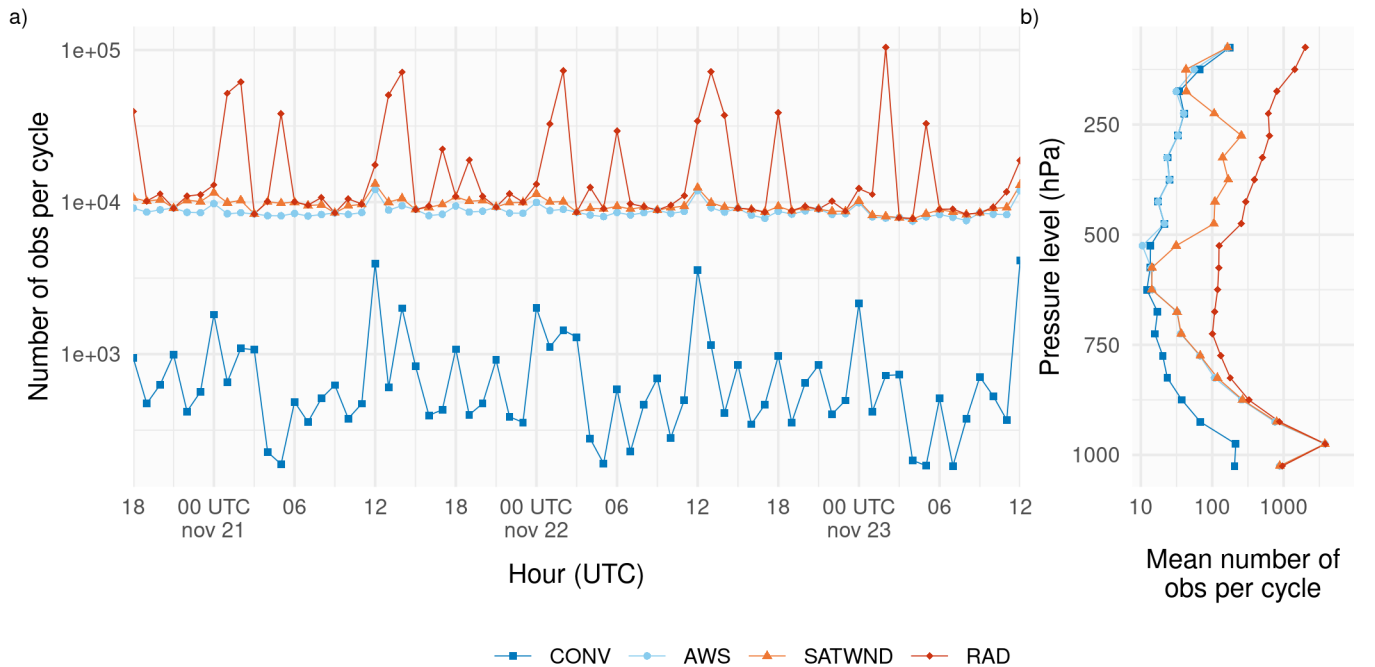


Figure 4: a) Number of assimilated observations per cycle and b) time averaged number of assimilated observations per cycle divided into 50 hPa-depth vertical layers for the CONV (blue squares and line), AWS (light blue dots and line), SATWND (orange triangles and line) and RAD (red diamonds and line) experiments.

257 the assimilation system were used for validation. The experiment period covers IOP
258 missions 7 and 8, during which 74 radiosondes were launched in a small area near the
259 center of the experimental domain (Figure 2b).

- 260 • The Satellite precipitation estimation IMERG Final Run with 0.01° spatial resolution
261 and 30 minutes temporal resolution (Huffman et al., 2018) was used as a reference
262 state to validate the skill of 1-hour forecasts to represent the precipitation over the
263 domain.
- 264 • Radar observations are used to perform a qualitative and visual assessment of the
265 convective features. The data comes from 9 radars located in the domain and is
266 provided by the Argentine C-band Doppler dual-polarization weather radar network
267 (de Elía et al., 2017) with a temporal frequency of 10 minutes. For this work, only
268 the maximum reflectivity in the column (COLMAX) closest to the analysis time was
269 used.

270 *2.4. Experimental design*

271 To investigate the impact of different observations upon the analysis, four DA experi-
272 ments were performed using different observation sets (Table 4). The CONV experiment
273 uses only conventional observations from PREPBUFR. In a second experiment, referred to
274 as AWS, all the observations included in CONV are assimilated plus the 10-minute frequency
275 surface observations from AWS. In the third experiment, referred to as SATWND, the ob-
276 servations from the AWS experiment along with the satellite-derived winds are assimilated.
277 Finally, a fourth experiment referred to as RAD assimilates all available clear-sky radiances
278 from sensors onboard polar orbiting satellites as described in section 2.3.4.

279 The horizontal distribution of the average number of assimilated observations per cycle
280 in each experiment is shown in Figure 3. The larger number of assimilated observations over
281 the center and east of the domain corresponds to the AWS observations. In Figure 4a the
282 number of assimilated observations over time is shown. Local maxima at 12 and 00 UTC
283 found mainly in CONV are attributed to operational soundings. The strong variability in

Table 4: Observation types assimilated in each experiment.

Obs type	CONV	AWS	SATWNDRAD
Conventional (PREPBUFR)	x	x	x
Conventional (AWS)		x	x
Satellite-derived winds		x	x
Radiances			x

284 the number of radiance observations per cycle is also noticeable and depends on the satellite
 285 coverage. The maxima at 13-14 and 01-02 UTC in RAD correspond to the contribution of
 286 the multispectral sensors. The vertical distribution of the mean number of observations per
 287 cycle (Figure 4b) shows a maximum in low levels due to the AWS observations. Satellite-
 288 derived winds are maximized at the upper troposphere (between 500-250 hPa). Above 850
 289 hPa, most of the observations correspond to radiance observations.

290 All the assimilation experiments start at 18 UTC Nov 20, 2018 and continue until 12
 291 UTC Nov, 23 (totaling 67 hours/assimilation cycles). The initial 60-member ensemble is
 292 generated as explained in section 2.2 from a spin-up run without assimilating observations
 293 performed between 12 UTC and 18 UTC Nov, 20 (Figure 5).

294 Ensemble forecasts initialized from the different analysis experiments at 00 and 06 UTC
 295 Nov 22 were performed to evaluate the impact of the different observing networks on short
 296 range precipitation forecasts. Both forecasts are integrated until 12 UTC Nov 23. All
 297 forecasts use the same domain and ensemble configuration as the analysis. The boundary
 298 conditions for the ensemble members are generated by adding random perturbations to the
 299 GFS deterministic forecast (0.25° horizontal grid spacing and 6-hour temporal resolution;
 300 National Centers for Environmental Prediction, National Weather Service, NOAA, U.S.
 301 Department of Commerce (2015)).

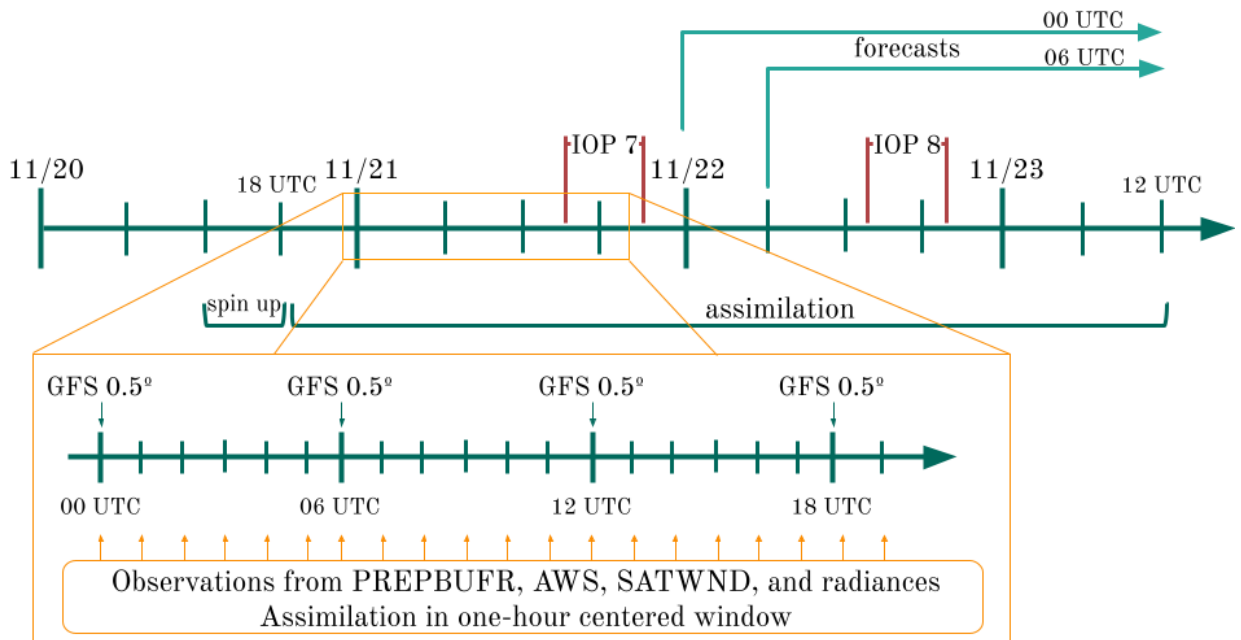


Figure 5: Diagram of the analysis cycles between 18 UTC Nov 20, and 12 UTC Nov 23 plus spin up period of 6 hours. The zoomed section shows the hourly assimilation that is performed within a one-hour centered window and new boundary conditions from GFS every 6 hours. The two IOP missions from the RELAMPAGO field campaign and the ensemble forecast initialized at 00 and 06 UTC Nov 22 are shown.

302 2.5. Verification methods

303 A set of metrics are selected to evaluate different aspects of the analysis obtained in
 304 the experiments conducted in this paper. These aspects include a validation of how the
 305 uncertainty is quantified in the first-guess and in the analysis, and how different experiments
 306 fit an independent set of observations that are not assimilated.

307 To evaluate the statistical consistency of the uncertainty quantification in the ensemble
 308 system the Reduced Centered Random Variable (RCRV, Candille et al. (2007)) is used which
 309 is defined as:

$$RCRV = \frac{m - x_o}{\sqrt{\sigma_o^2 + \sigma^2}} \quad (2)$$

310 where x_o is the assimilated observation and its error σ_o , the ensemble mean of the analysis
 311 in observational space m , and the standard deviation σ of the ensemble. The $RCRV$ is the
 312 ratio of the distance between the observations and the forecast and its expected standard
 313 deviation assuming the statistical independence between the forecast error (estimated from
 314 the ensemble spread) and the observation error. The average of $RCRV$ computed over all
 315 the analysis cycles represents the bias of the ensemble mean with respect to the observations
 316 normalized by the estimated uncertainty:

$$meanRCRV = E[RCRV] \quad (3)$$

317 If the ensemble has a positive bias, $meanRCRV$ will be positive, on the opposite, if the
 318 ensemble has a negative bias, $meanRCRV$ will be negative. The standard deviation of the
 319 $RCRV$ or $sdRCRV$ is defined as:

$$sdRCRV = \sqrt{\frac{1}{M-1} \sum_{i=1}^M (RCRV_i - meanRCRV)^2} \quad (4)$$

320 where M is the ensemble size. The $sdRCRV$ measures how large is the distance between
 321 the forecast and the observations with respect to the expected distance (given by the com-
 322 bination of the ensemble spread and the observation error). Assuming that the observation

323 error is accurately estimated, an $sdRCRV > 1$ indicates that the ensemble is underdisper-
 324 sive (i.e. the distance between the observations and the forecasts is larger than expected),
 325 and an $sdRCRV < 1$ indicates that the ensemble is overdispersive (i.e. the distance between
 326 the observations and the forecasts is lower than expected). A consistent system will have
 327 no bias ($meanRCRV = 0$) and a standard deviation equal to 1 ($sdRCRV = 1$).

328 The fit of the first-guess and analysis to a set of independent observations, the high-
 329 resolution radiosondes from RELAMPAGO, is computed based on the Root Mean Square
 330 Error (RMSE) and the BIAS:

$$RMSE = \sqrt{\frac{1}{N} \sum_{i=1}^N (X_i - O_i)^2} \quad (5)$$

$$BIAS = \frac{1}{N} \sum_{i=1}^N (X_i - O_i) \quad (6)$$

331 where O and X stand for independent observations and the simulations respectively, and
 332 N is the sample size.

333 For the comparison of the first-guess precipitation with the IMERG precipitation esti-
 334 mates, the Fractions Skill Score (FSS, Roberts (2008)) is computed for different neighbor-
 335 hood length scales and thresholds:

$$FSS = 1 - \frac{\sum_{i=1}^N (P_{xi} - P_{oi})^2}{\sum_{i=1}^N (P_{xi})^2 + \sum_{i=1}^N (P_{oi})^2} \quad (7)$$

336 where P_{oi} is the fraction of grid points in the i -th sampling area in which the observed
 337 accumulated precipitation is greater than a specified threshold. Following Roberts et al.
 338 (2020), P_{xi} is calculated from the ensemble probability precipitation over the same threshold
 339 in each grid point by averaging over the i -th sampling area. The FSS was computed from
 340 the accumulated precipitation over 6 hr rolling windows by adding the 1-hr accumulated
 341 precipitation forecasts over 6 consecutive assimilation cycles.

342 2.6. Computation procedures

343 All the experiments were performed at the National Center for Atmospheric Research
 344 (NCAR) supercomputer Cheyenne (Computational and Information Systems Laboratory,

345 2019). All the analyses in this paper were conducted using the R programming language
346 (R Core Team, 2020), using data.table (Dowle and Srinivasan, 2020) and metR (Campitelli,
347 2020) packages. All graphics are made using ggplot2 (Wickham, 2009) and the paper was
348 rendered using knitr and rmarkdown (Xie, 2015; Allaire et al., 2019).

349 3. Results

350 3.1. Ensemble consistency

351 To investigate the ability of the first-guess ensemble mean to fit the observations taking
352 into account the uncertainties of the forecast and the observations, the *meanRCRV* and the
353 *sdRCRV* is calculated for the RAD experiment. As this experiment assimilates all types
354 of observations used in this work, it is possible to analyze the consistency of the ensemble
355 by comparing it with each type of observation. Figure 6 shows the *sdRCRV* for surface
356 observations box-averaged to a 2.5° grid. The *sdRCRV* for wind observations (Figure 6a) is
357 close to 1 suggesting a good agreement between the ensemble spread, the forecast error, and
358 the observation error. For the temperature (Figure 6b), the results are similar except that
359 for some areas in the west of the domain the *sdRCRV* can be as high as 4.5. These higher
360 values of *sdRCRV* can be associated with systematic errors arising from high differences
361 between the model surface and the observations. Small scale circulations associated with
362 the complex terrain and not well resolved by the model can also contribute to increase the
363 distance between the forecast and the observations. These aspects are usually not captured
364 by the ensemble spread unless a well tuned space dependent inflation scheme is used thus
365 leading to greater sdRCRV values.

366 Figure 7 shows the mean and standard deviation of the RCRV for the upper-air ob-
367 servations. Figures 7a-b show the RCRV statistics for soundings (ADPUPA) and aircraft
368 (AIRCAR and AIRCFT). Both ADPUPA and AIRCFT show a generally good agreement
369 between the ensemble spread and the observation error. As sounding observations and their
370 associated errors are known to be reliable, this result indicates that the ensemble has an ap-
371 propriate spread. AIRCAR presents an irregular profile with *sdRCRV* values that suggest

372 that the error for this type of observation is overestimated. ADPUPA and AIRCAR present
373 a *meanRCRV* profile near zero at middle and upper levels. At low levels, the *meanRCRV*
374 profile is positive, showing a cold bias present in the model, a characteristic already studied
375 in Ruiz et al. (2010) and Dillon et al. (2021).

376 Satellite-derived winds observations vary in number depending on the satellite and the
377 level. In Figure 7c only the *RCRV* calculated with at least 100 observations for each satellite
378 and level is included. At low levels, where there are not many observations available, the
379 profiles of *meanRCRV* and *sdRCRV* show a larger departure from the expected behavior
380 with a negative bias, and a possible overestimation of the observation error. Wind estima-
381 tions derived from water vapor channels are abundant above 500 hPa where their bias is
382 close to zero. The only exception are the EUMETSAT observations which contribute very
383 little in the region.

384 The mean *RCRV* profiles calculated from the radiance observations (Figure 7d) show
385 almost no bias and the same happens if the *meanRCRV* is calculated over each channel of
386 each sensor (not shown). This indicates that the bias correction algorithm works as expected.
387 The *sdRCRV* values are less than 1 for all sensors possibly due to an overestimation of the
388 observation errors to reduce the influence of potentially erroneous observations.

389 Overall, these results indicate that the ensemble spread is consistent with the short-range
390 forecast error and that systematic errors are relatively small for most of the observation types
391 used in this work. Moreover, these results suggest the relaxation-to-prior spread inflation
392 parameter $\alpha = 0.9$ is adequate for the system.

393 3.2. Impacts of assimilated observations

394 This section presents the impact of assimilating different observation types on variables
395 which are particularly relevant for the occurrence of deep moist convection. The analysis is
396 performed over a smaller domain (red box in Figure 2a) to focus on the region most directly
397 affected by the MCS. Figures 8a-c show the analysis difference between experiments in the
398 spatially averaged vertical profile of temperature. By averaging the differences between two
399 experiments the systematic impact produced by different observing systems on the analyzed

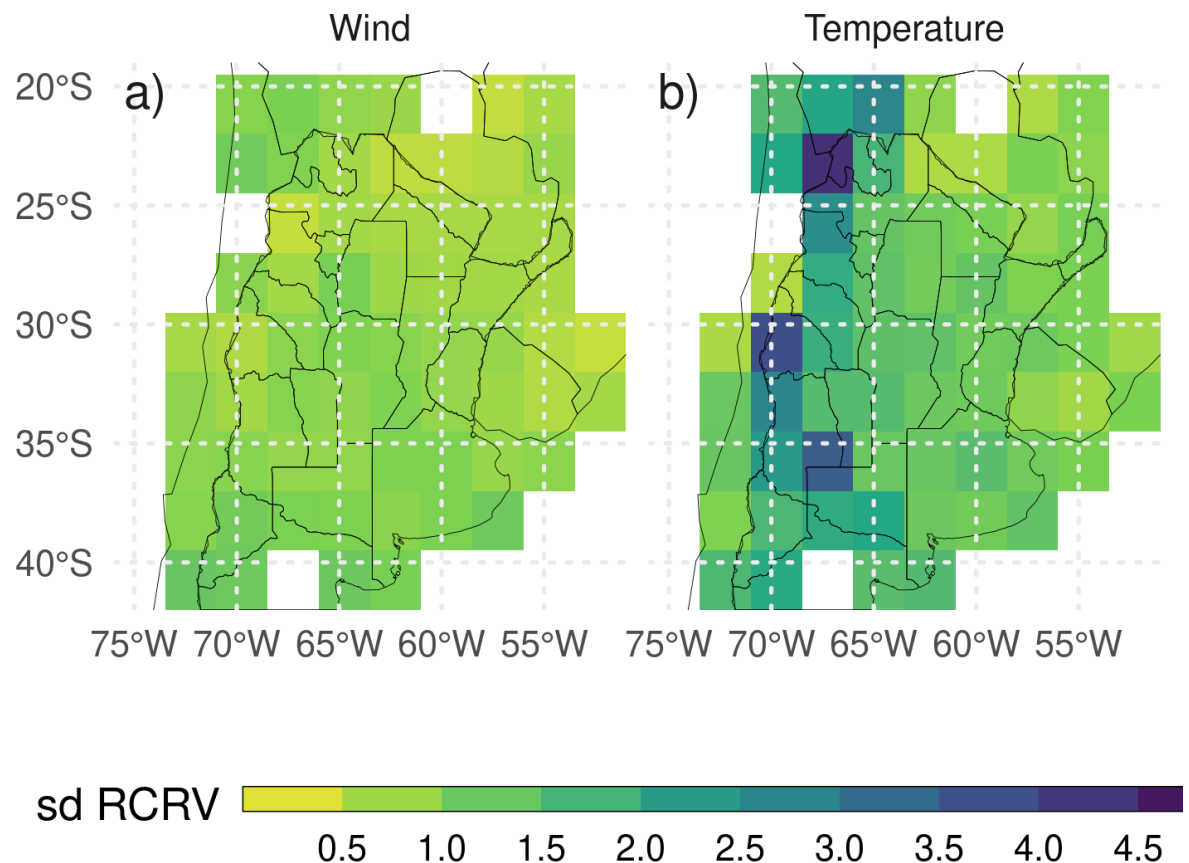


Figure 6: First guess *sdRCRV* calculated for surface observations (from PREPBUFR and AWS) of a) wind, and b) temperature averaged over 2.5° boxes for the RAD experiment. Observations were aggregated every hourly cycle for the entire experiment period.

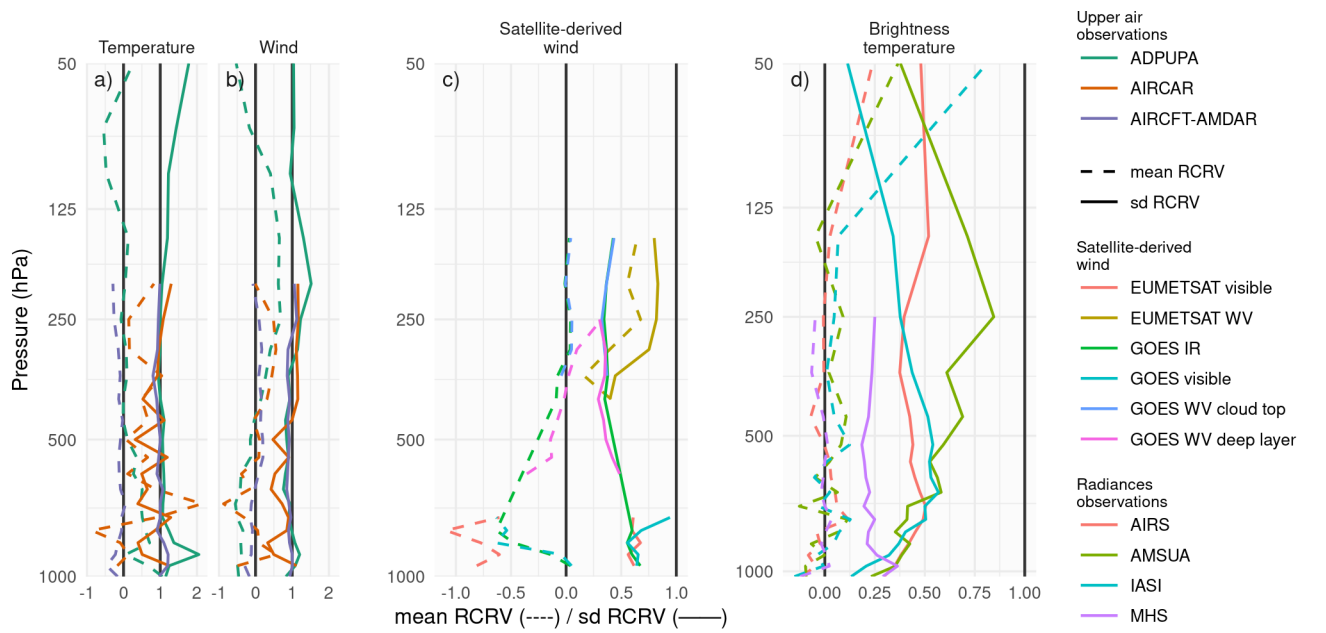


Figure 7: Vertical profiles of first guess *meanRCRV* (dashed line) and *sdRCRV* (solid line) for a) temperature and b) wind of sounding and aircraft observations, c) satellite-derived wind observations, and d) brightness temperature observations for the RAD experiment. Observations were aggregated every hourly cycle for the entire experiment period.

state can be isolated. During the first day, the assimilation of AWS observations results in a colder PBL. This cooling effect has a clear diurnal cycle, being stronger during nighttime (Figure 8a). During the second day of the experiment, the impact of AWS observations extends into the middle and upper troposphere coinciding with the mature stage of the MCS. The warm difference shown in AWS-CONV between 500 and 200 hPa is produced by the development of stronger convection in AWS compared to CONV. This is a good example of how low-level information provided by surface weather stations can rapidly spread into the troposphere in the presence of deep moist convection. Although the mid-to-upper circulation can have an important impact on the organization and evolution of the MCS over the region, the satellite-derived winds did not have an appreciable impact on the mean temperature and humidity (Figure 8b-e), possibly due to the large observation errors used for the assimilation. During the first day of the experiment, the assimilation of radiances produces a warming effect in the PBL which partially compensates for the cooling effect of AWS observations (Figure 8c). No clear systematic impact is found above the PBL during this period. During the second day, the impact of radiance observations is found through the troposphere with a distribution that is similar to the impact found in the AWS experiment but with the opposite sign.

Comparing the specific humidity in the experiments (Figures 8d-f), the impact of assimilating AWS with fine spatial and temporal resolution is most substantial at low levels (Figure 8d). The PBL in the AWS experiment is consistently moister than in the CONV experiment, particularly at nighttime. The increase in low-level moisture by a denser surface network is consistent with previously reported dry biases in the WRF model over the region (Casaretto et al., 2022, Matsudo et al. (2021), Ruiz et al. (2010)). The moistening of the PBL is mainly driven by the covariance between temperature and specific humidity within the PBL. In the experiment and over the center of the domain, this covariance remains negative, increasing low-level moisture as the observations introduce negative temperature corrections. As for the temperature, the systematic impact of satellite-derived winds on moisture is small (Figure 8e). Figure 8f shows that radiances reduce low-middle level moisture during the first day of the experiment. The drying effect extends to lower-middle levels during the second

429 day of the experiment coinciding with the development of the MCS between 00 and 12 UTC
 430 Nov 22.

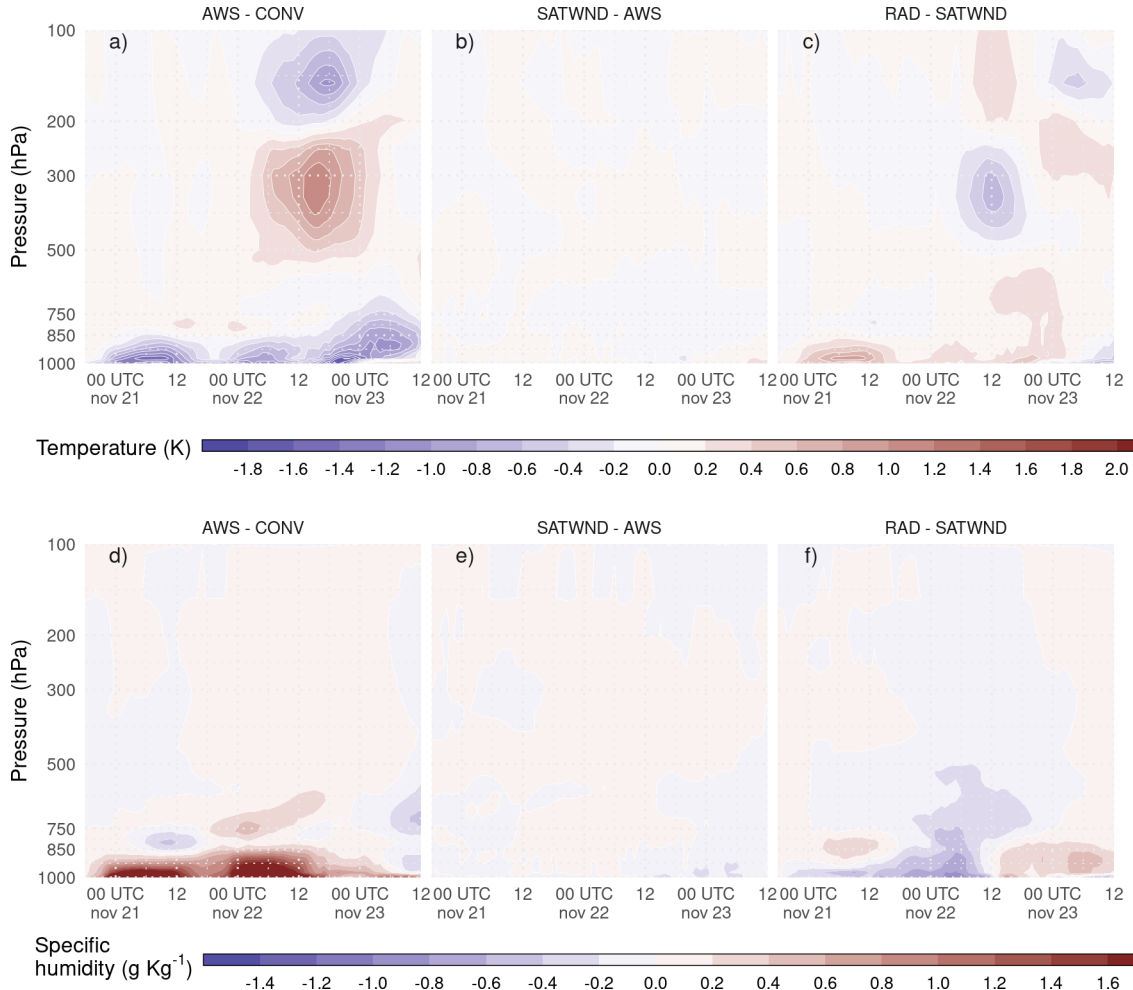


Figure 8: Difference between analysis ensemble mean experiments a) and d) AWS-CONV, b) and e) SATWND-AWS, and c) and f) RAD-SATWND for the spatially averaged vertical profiles of temperature (a, b, and c, in K) and specific humidity (d, e, and f in g kg^{-1}) calculated over the inner domain (red box in Figure 2a) for each analysis cycle.

431 The impacts on the wind components are shown in Figure 9, along with the correspond-
 432 ing averaged wind component in the experiment with the largest number of assimilated
 433 observations (for example, Figure 9a shows the zonal wind difference between AWS and
 434 CONV and the zonal wind for AWS). The assimilation of AWS produces a more easterly
 435 wind and a less northerly wind at low levels during the first two days of analysis (Figures

9a,b). There is a diurnal cycle in the impact of surface weather stations on the meridional velocity (Figure 9d) with a stronger reduction of the northerly wind during night hours. This indicates that surface observations are reducing the intensity of the low level jet present in the pre-convective environment. After 18 UTC Nov 22, the opposite effect is observed when the MCS is moving through the domain to the northeast. After the initiation of the convective cells, the systematic impact on the wind field is larger at mid and upper levels (Figures 9d, f). During Nov 22 and 23 the impact of assimilating AWS observations produces an increase of northerly wind in upper levels. This could be a consequence of a stronger MCS with an increased polar side upper level outflow. Although satellite-derived wind observations produce the largest impact in mid-to-upper levels where the number of observations is largest; the systematic impact is overall smaller than the one produced by assimilating data from AWS (Figures 9b, e). The reason of the small impact observed in SATWND could be associated to the large observation error used for satellite-derived wind observations.

The assimilation of radiances produces a reduction in the westerly wind compared with respect to SATWIND in low and upper levels (Figure 9c). For the meridional wind, these observations produce an enhancement on average of the northerly low-level flow of 1ms^{-1} , opposite to what is generated by the assimilation of AWS observations during the nights, between 03 and 12 UTC, previous to the development of the MCS (Figure 9f). At upper levels and during Nov 22 and 23 the average impact of assimilating radiances is a decrease in the wind speed. The meridional wind field at 200 hPa at different times shows that the outflow from the MCS is even more intense than in the other experiments, while the southerly wind ahead of the MCS also increases producing an average reduction of the northerly wind (Figure 9f).

The difference between ERA5 reanalyses (Hersbach et al., 2018, ‘) and the ensemble mean analyses are also compared in Figure 10, which supports Figures 8 and 9. Specifically, Figure 10a shows a warm bias in low levels (i.e. CONV is warmer than ERA5) that decreases in Figure 10b when the AWS observations are assimilated. In the same direction, Figure 8a shows a negative difference between AWS and CONV meaning that the AWS observations are cooling the low levels. Comparing ERA5-RAD (Figure 10d), there is a small increase

465 in the warm bias, associated with the warming produced by the radiance observations as
466 shown in Figure 8c. A similar effect can be observed for specific humidity, AWS observa-
467 tions partially correct the dry bias present in Figure 10e and the assimilation of radiance
468 observations reduces the positive impact of AWS. The impact on the wind components is
469 minor so only the meridional wind is included in Figures 10i-l, which show that the radiance
470 observations are mainly responsible for the positive impact observed in the analysis by re-
471 ducing the distance ERA5-RAD, particularly during the mature stage of the MCS. Overall,
472 the adjustments due to assimilating radiance and AWS observations lead to an ensemble
473 mean analyses closer to ERA5 reanalyses.

474 To investigate how changes in the PBL can modify the pre-convective environment, the
475 analysis mean horizontal distribution of the low level northerly flow (for the first 7 sigma
476 levels), precipitable water, low level temperature, and CAPE are compared. At 00 UTC
477 Nov 22 (after 30 assimilation cycles) the first convective cells were developing over the
478 southern region of the domain along the cold front. Figure 11a shows the precipitable water
479 (shaded) and the vertically averaged low-level meridional wind component (contours). It
480 shows that the moist tongue extending over the northern part of the domain is enhanced by
481 the assimilation of denser surface observations. The moisture increase is particularly strong
482 at the southern tip of this tongue, just ahead of the cold front where convection initiation was
483 taking place. AWS and SATWND experiments are very similar, with values of precipitable
484 water over 55 kg m^{-2} north of 30°S and a similar vertical distribution of specific humidity (not
485 shown). RAD has lower precipitable water content than AWS and SATWND, but higher
486 than CONV. The distribution of moisture at low levels in RAD seems to be the result of the
487 combination of the moistening effect of assimilating AWS – partially compensated by the
488 assimilation of radiance observations – and a reduced meridional moisture transport due to
489 the weaker northerly flow over the center of the domain compared to CONV.

490 The analyzed distribution of temperature and moisture in the PBL (Figure 11b) re-
491 sembles the characteristics observed in the temperature profiles (Figure 8a-c) where AWS
492 produces a colder PBL than CONV while the PBL in RAD is warmer than in SATWND. On
493 average the PBL in AWS and SATWND is colder than in CONV, while RAD shows a warmer

494 PBL than AWS due to the assimilation of radiance observations. A warmer PBL increases
495 the potential instability and helps to generate a suitable environment for the development of
496 deep convection. Figure 11c shows the most unstable convective available potential energy
497 (CAPE, shaded) and the 0 to 6 km wind shear. The values of CAPE in CONV do
498 not exceed 2000 J Kg^{-1} while the rest of the experiments show maximum CAPE over
499 4000 J Kg^{-1} . CAPE in the RAD experiment is lower compared to AWS or SATWND.
500 This is consistent with less humidity in the PBL with respect to these experiments but may
501 be partially compensated by a slightly warmer PBL in the RAD experiment. The 0-6 km
502 wind shear is more intense in AWS, SATWND, and RAD reaching values over 15 m s^{-1} at
503 the southern tip of the region with positive CAPE values. Moreover, in this same region,
504 these experiments show larger CAPE values than CONV. Note that wind shear over 15
505 m s^{-1} is associated with the development of more intense and organized MCSs (Chen et al.,
506 2015) and also with conditions favorable for supercells (Markowski and Richardson, 2010).

507 3.3. Validation against independent observations

508 First, the impact of assimilating different observation types in terms of the representation
509 of the MCS and its associated precipitation is analyzed. Figure 12a shows the hourly ac-
510 cumulated precipitation as estimated by IMERG, and the probability matched mean (PM)
511 (Clark, 2017) for the first-guess hourly accumulated precipitation as averaged between 67°W
512 and 54.5°W as a function of time and latitude in the different experiments. The heaviest
513 precipitation (over 12 mmh^{-1}) starts during the afternoon of Nov 22 and continues during
514 Nov 23 after the end of the simulated period (Figure 12a). In all the experiments, the ac-
515 cumulated precipitation in the short-range forecasts is underestimated. This is particularly
516 evident in CONV (Figure 12b), where the convection initiation is delayed and occurs further
517 north with respect to the observed initiation. AWS, SATWND, and RAD better capture the
518 timing and location of convective initiation (Figures 12c-e). AWS and RAD show a more
519 fragmented distribution compared with SATWND, possibly due to the development of less
520 organized convection during Nov 22. After 18 UTC Nov 22, RAD shows improvements in
521 the precipitation rate and its distribution compared to the other experiments as a result of

522 enhanced development of the convection.

523 The FSS is computed to quantify the spatial match between the observed precipitation
524 and the first-guess hourly accumulated precipitation for the different experiments (Figure
525 13). For each threshold and spatial scale, Equation @red(eq: eq7) is applied in 6-hours
526 rolling windows throughout the experiment period. All experiments show similar values of
527 FSS during the initiation of the convection before 06 UTC Nov 22 except for RAD which
528 performs better than the rest of the experiments during this period. This indicates that
529 radiance observations have a positive impact on the analysis. The FSS for CONV is the
530 lowest compared to the rest of the experiments and the differences are larger during the
531 mature stage of the MCS. AWS and SATWND show similar FSSs indicating that satellite-
532 derived wind assimilation has little impact on the precipitation for this case study. The
533 assimilation of radiances led to an overall improvement of the 1-hour forecast precipitation,
534 particularly for the 25 mm threshold during the period of heaviest precipitation on Nov 22
535 (Figure 13b,d). The enhancement is also important at the developing stage of the MCS
536 (between 00 and 12 UTC Nov, 22 and also for spatial scales above 500 km, not shown).

537 To complement the analysis, Figure 14 shows the observed maximum reflectivity in
538 the vertical column (COLMAX) and the ensemble mean COLMAX for the CONV and
539 RAD experiments at different times between 10 and 19 UTC Nov 22. These experiments
540 were chosen because they represent the analysis with the minimum (CONV) and maximum
541 (RAD) number of assimilated observations. In addition, they are the worst (CONV) and best
542 (RAD) performing experiments in terms of the 1-hour precipitation forecast skill (Figure 13).
543 Overall, none of the short-range forecasts capture the mesoscale details in the reflectivity
544 distribution. This is partially expected considering the coarse horizontal grid spacing (10
545 km), which is not enough to appropriately represent the strength of the convective band
546 associated with the MCS. RAD better represents the observed features of the system showing
547 a stronger and more organized MCS than CONV, over the domain center at 10 and 13 UTC
548 (first and second columns in Figure 14). The convective cells that initiate after 16 UTC along
549 the warm front in the northeast part of the domain are well captured by both experiments
550 but are better represented in terms of strength in RAD. In addition, CONV captures the

551 location of the MCS, but the convection seems to be less organized and much weaker than
552 in RAD. Before and after the times shown in Figure 14, the agreement between location
553 of the observed convective cells and the simulated in the experiment is quite good in the
554 regions where radar data are available, especially for RAD.

555 Finally, Figure 15 shows the RMSE and bias calculated by comparing the experiments
556 with radiosonde data from the RELAMPAGO missions, IOP 7 from 15 to 21 UTC Nov 21
557 (including 30 radiosondes), and IOP 8 from 14 to 20 UTC Nov 22 (including 22 radiosondes).

558 IOP 7 (Figures 15a-d) provides a good characterization of the pre-convective environment
559 during the first day of our experiments. The area where the observations were taken was
560 characterized by mostly clear skies and a low-level northerly flow associated with warm and
561 moist advection. In general, the experiments show a similar RMSE and bias for all the
562 variables. AWS observations were able to reduce the RMSE for temperature and dew point
563 temperature in the PBL and reduce a small dry bias. However, in this region (Figure 2b)
564 and for this period, AWS increments (Figure 9d) degrades the zonal wind between 7 and 12
565 km increasing the bias and RMSE (Figure 15c).

566 For IOP 8 (Figures 15e-h), the densely observed area was behind the MCS, but far
567 enough from it to not be directly affected by its mesoscale circulation. This area was also
568 behind the cold front and affected by low-level cold advection. The assimilation of AWS,
569 SATWND, and RAD reduces the cold bias and RMSE for temperature between 5 and 12
570 km and the RMSE in the PBL compared with CONV (Figure 15e). The reduction of
571 bias and RMSE is also important for dew point temperature (Figure 15f) with SATWND
572 showing the biggest impact followed by AWS and RAD. The zonal wind is overestimated
573 in the analyses and only RAD shows an improvement with respect to CONV in the upper
574 troposphere (Figure 15g). At low levels the meridional wind (Figure 15g) presents a negative
575 bias, indicating an underestimation of the southerly wind behind the cold front principally
576 in AWS, SATWND, and RAD. In fact, low level biases in these experiments are higher
577 than in the CONV experiment, indicating a detrimental effect of the additional observations
578 (possibly associated with the effect of AWS).

579 *3.4. Ensemble forecast validation*

580 This section analyzes the 60-member ensemble forecast initialized at 00 and 06 UTC
581 Nov 22 from each experiment that runs for 36 and 30 h respectively, until 12 UTC Nov 23.
582 The FSS is again calculated for the ensemble forecasts in 6-hour rolling windows for the
583 same thresholds and spatial scales as for the first-guess hourly accumulated precipitation
584 to quantify the skill of the forecasts to predict precipitation (Figure 16). CONV forecasts
585 perform very poorly in terms of the FSS compared with the experiments that include other
586 sources of observations. AWS, SATWND, and RAD show improvements in the FSS values,
587 particularly for the higher threshold (Figure 16b, d). Moreover, the late initialization at
588 06 UTC performs better for AWS, SATWND, and RAD than the forecast initialized at 00
589 UTC, highlighting the positive impact of the observations assimilated between 00 and 06
590 UTC.

591 The satellite-derived wind observations show a clearly positive impact on the forecast, in
592 contrast to what was seen when comparing the 1-h forecast with independent observations
593 in terms of precipitation. Conversely, the radiance observations resulted in a neutral to a
594 slightly negative impact on the forecast as opposed to what was seen when comparing the
595 1-h forecast to IMERG estimations. The reason why the forecasts initialized from RAD
596 degrade over time needs to be further study. However, it is possible that the assimilation of
597 observations associated with channels affected by the surface is contributing to the degrada-
598 tion of the PBL in the analysis and subsequently in the forecasts. Lim et al. (2014) observed
599 limited impact when assimilating AIRS observations and attribute this result to the use of
600 surface channels where the uncertainties associated with emissivity are large.

601 **4. Conclusions**

602 Southern South America is a particularly interesting region due to the heterogeneity in
603 topography and coarse resolution of the operational observing network (considering both
604 surface based and upper air observations). This, combined with a climatology characterized
605 by frequent organized convective events makes mesoscale DA particularly challenging. This

606 paper investigates, for the first time in South America, using a case-study approach, the
607 impact of different observation systems on the performance of an ensemble-based mesoscale
608 regional DA system. This case study corresponds to a massive MCS that developed over
609 Southern South America on Nov 22, 2018 during the RELAMPAGO field campaign. In
610 particular, the impact on the analysis quality of assimilating frequent and relatively dense
611 surface observations, satellite-derived winds, and satellite clear-sky radiances from multiple
612 sensors is explored.

613 Firstly, the consistency of the ensemble was evaluated to ensure a good agreement be-
614 tween the ensemble spread and the observational errors with respect to the distance between
615 the ensemble mean and the observations. While conventional observations departures are
616 consistent with the ensemble spread and assumed observation errors, satellite-derived winds
617 and radiance observations departures are lower than expected. The latter could be the re-
618 sult of an overestimation of the observation errors which is usually introduced to avoid the
619 detrimental impact on the analysis of poor quality observations. In this case study, all the
620 observation types considered (i.e. automatic weather stations, satellite derived winds and
621 clear-sky radiances from polar orbiting satellites) improves the quality of the analysis and
622 of the short range forecast with respect to the conventional observation network. In terms
623 of the analysis, automatic weather station observations, which have high spatial and tem-
624 poral resolution, produced impacts mainly within the PBL but which occasionally extends
625 throughout the troposphere during the periods where moist convection is stronger within
626 the domain. These observations also helped to reduce the warm and dry bias present in the
627 model, producing an analysis closer to the ERA5 reanalysis. During the pre-convective en-
628 vironment, assimilating surface temperature, dew point temperature, and meridional wind
629 improved the analysis at low levels when compared with observed soundings. In particular,
630 when these observations are assimilated, precipitable water content and low level meridional
631 circulation led to the enhancement of deep convection and heavy precipitation which is closer
632 to observations.

633 Positive results were also found when assimilating radiance observations, which produced
634 a better development of the convection and its associated outflow circulation, mainly during

635 the mature stage of the MCS, leading to increased accumulated precipitation compared to the
636 case in which these observations are not assimilated. However, these observations weakened
637 the impact of automatic weather station observations within the PBL, slightly increasing
638 the warm and dry bias with respect to ERA5. While this needs to be further studied,
639 it could be related to the assimilation of channels affected by the surface or sub-optimal
640 bias correction. Comparing the experiment with independent soundings, the assimilation of
641 radiances improved mid and upper level wind.

642 The assimilation of satellite-derived wind did not produce a noticeable impact on the
643 analysis. This is possibly due to the relatively small number of observations in low levels
644 available for this case study and their large observation error. However, there are improve-
645 ments in the 1-h forecast accumulated precipitation distribution. A more comprehensive
646 analysis is necessary to understand the mechanisms behind the impact of these observations
647 on longer range forecasts.

648 The evaluation of the performance of independent ensemble precipitation forecasts ini-
649 tialized from the analyses during Nov 22 showed that the forecasts initialized from AWS,
650 SATWND, and RAD were able to forecast the precipitation substantially better than CONV.
651 In particular, continuous assimilation of satellite-derived wind and radiance observations
652 improved the latest initialization but only satellite-derived wind observations produced a
653 positive impact that persisted throughout the forecast. Why the forecast initialized from
654 RAD did not perform better than SATWND needs to be further study.

655 To summarize, in this case study we found that the assimilation of surface observations
656 with high spatial and temporal resolution, satellite-derived winds, and clear-sky radiances
657 from polar orbiting satellites had an overall positive impact on the development of the
658 studied MCS and its associated precipitation. Moreover, ensemble forecasts initialized from
659 the analysis showed promising results for predicting extreme severe precipitation events.
660 In the future, we will further analyze the impact of these observations upon short-range
661 forecasts over longer periods and evaluate the assimilation of other sources of observations
662 such as GPS radio occultation data and radiances from geostationary orbiting satellites like
663 GOES-16.

664 **5. Code and data availability**

665 A version-controlled repository of the code used to create this analysis, including the code
666 used to download the data can be found at <https://github.com/paocorralles/mesoda>.
667 The derived data that support the findings of this study are also openly available in Zenodo
668 at <http://doi.org/10.5281/zenodo.7015913>, version 0.9.2.

669 **Acknowledgments**

670 We are very thankful to the Atmospheric and Sea Research Center (CIMA), the Uni-
671 versity of Buenos Aires (UBA), and the National Scientific and Technical Research Council
672 (CONICET) who support this study. We acknowledge the Sistema Nacional de Radares
673 Meteorológicos supported by the Secretaría de Infraestructura y Política Hídrica for kindly
674 providing the radar observations used for validation and the National Meteorological Service
675 for facilitating the access to the data. We also acknowledge the Cheyenne HPC resources
676 (doi:10.5065/D6RX99HX) from NCAR’s Computational and Information Systems Labora-
677 tory, National Science Foundation (project code UIUC0012). Also, PICT 2017-2233 and
678 PICT 2018-3202 projects of the National Agency for the Promotion of Research, Technolog-
679 ical Development and Innovation from Argentina partially funded this project.

680 **References**

- 681 JJ Allaire, Jeffrey Horner, Yihui Xie, Vicent Martí, and Natacha Porte. *Markdown: Render Markdown with*
682 *the c Library 'Sundown'*, 2019.
- 683 Jeong-Ho Bae and Ki-Hong Min. Forecast Characteristics of Radar Data Assimilation Based on the Scales
684 of Precipitation Systems. *Remote Sensing*, 14(3):605, January 2022. ISSN 2072-4292. doi: 10.3390/
685 rs14030605.
- 686 Ivette H. Banos, Will D. Mayfield, Guoqing Ge, Luiz F. Sapucci, Jacob R. Carley, and Louisa Nance.
687 Assessment of the data assimilation framework for the Rapid Refresh Forecast System v0.1 and impacts
688 on forecasts of convective storms. *Geoscientific Model Development Discussions*, pages 1–36, October
689 2021. ISSN 1991-959X. doi: 10.5194/gmd-2021-289.
- 690 Y. Bao, J. Xu, A. M. Powell Jr., M. Shao, J. Min, and Y. Pan. Impacts of AMSU-A, MHS and IASI
691 data assimilation on temperature and humidity forecasts with GSI-WRF over the western United States.

- 692 *Atmospheric Measurement Techniques*, 8(10):4231–4242, October 2015. ISSN 1867-8548. doi: 10.5194/
693 amt-8-4231-2015.
- 694 A. Beck, B. Ahrens, and K. Stadlbacher. Impact of nesting strategies in dynamical downscaling of reanalysis
695 data. *Geophysical Research Letters*, 31(19), 2004. ISSN 1944-8007. doi: 10.1029/2004GL020115.
- 696 Harold E Brooks, James W Lee, and Jeffrey P Craven. The spatial distribution of severe thunderstorm and
697 tornado environments from global reanalysis data. *Atmospheric Research*, 67–68:73–94, July 2003. ISSN
698 01698095. doi: 10.1016/S0169-8095(03)00045-0.
- 699 Elio Campitelli. metR: Tools for Easier Analysis of Meteorological Fields, April 2020.
- 700 G. Candille, C. Côté, P. L. Houtekamer, and G. Pellerin. Verification of an Ensemble Prediction System
701 against Observations. *Monthly Weather Review*, 135(7):2688–2699, July 2007. ISSN 0027-0644, 1520-0493.
702 doi: 10.1175/MWR3414.1.
- 703 Gimena Casaretto, Maria Eugenia Dillon, Paola Salio, Yanina García Skabar, Stephen W. Nesbitt, Russ S.
704 Schumacher, Carlos Marcelo García, and Carlos Catalini. High-Resolution NWP Forecast Precipitation
705 Comparison over Complex Terrain of the Sierras de Córdoba during RELAMPAGO-CACTI. *Weather and
706 Forecasting*, 37(2):241–266, February 2022. ISSN 1520-0434, 0882-8156. doi: 10.1175/WAF-D-21-0006.1.
- 707 Daniel J. Cecil and Clay B. Blankenship. Toward a Global Climatology of Severe Hailstorms as Estimated by
708 Satellite Passive Microwave Imagers. *Journal of Climate*, 25(2):687–703, January 2012. ISSN 0894-8755,
709 1520-0442. doi: 10.1175/JCLI-D-11-00130.1.
- 710 Weiguang Chang, Dominik Jacques, Luc Fillion, and Seung-Jong Baek. Assimilation of Hourly Surface
711 Observations with the Canadian High-Resolution Ensemble Kalman Filter. *Atmosphere-Ocean*, 55(4-5):
712 247–263, October 2017. ISSN 0705-5900. doi: 10.1080/07055900.2017.1384361.
- 713 Fei Chen and Jimy Dudhia. Coupling an Advanced Land Surface–Hydrology Model with the Penn
714 State–NCAR MM5 Modeling System. Part I: Model Implementation and Sensitivity. *Monthly Weather
715 Review*, 129(4):569–585, April 2001. ISSN 1520-0493, 0027-0644. doi: 10.1175/1520-0493(2001)129<0569:
716 CAALSH>2.0.CO;2.
- 717 Qian Chen, Jiwen Fan, Samson Hagos, William I. Gustafson, and Larry K. Berg. Roles of wind shear at
718 different vertical levels: Cloud system organization and properties. *Journal of Geophysical Research:
719 Atmospheres*, 120(13):6551–6574, 2015. ISSN 2169-8996. doi: 10.1002/2015JD023253.
- 720 Xingchao Chen, Kun Zhao, Juanzhen Sun, Bowen Zhou, and Wen-Chau Lee. Assimilating surface obser-
721 vations in a four-dimensional variational Doppler radar data assimilation system to improve the analysis
722 and forecast of a squall line case. *Advances in Atmospheric Sciences*, 33(10):1106–1119, October 2016.
723 ISSN 0256-1530, 1861-9533. doi: 10.1007/s00376-016-5290-0.
- 724 T. Cherubini, S. Businger, C. Velden, and R. Ogasawara. The Impact of Satellite-Derived Atmospheric
725 Motion Vectors on Mesoscale Forecasts over Hawaii. *Monthly Weather Review*, 134(7):2009–2020, July

- 726 2006. ISSN 1520-0493, 0027-0644. doi: 10.1175/MWR3163.1.
- 727 Adam J. Clark. Generation of Ensemble Mean Precipitation Forecasts from Convection-Allowing Ensembles.
728 *Weather and Forecasting*, 32(4):1569–1583, August 2017. ISSN 1520-0434, 0882-8156. doi: 10.1175/WAF-
729 D-16-0199.1.
- 730 Computational and Information Systems Laboratory. Cheyenne: HPE/SGI ICE XA System (University
731 Community Computing). *National Center for Atmospheric Research Boulder, CO*, 2019. doi: doi:10.
732 5065/D6RX99HX.
- 733 Ramón de Elía, Luciano Vidal, and Pedro Lohigorry. El SMN y la red argentina de radares meteorológicos.
734 <http://hdl.handle.net/20.500.12160/625>, 2017.
- 735 María E. Dillon, Yanina García Skabar, Juan Ruiz, Eugenia Kalnay, Estela A. Collini, Pablo Echevarría,
736 Marcos Saucedo, Takemasa Miyoshi, and Masaru Kunii. Application of the WRF-LETKF Data Assimi-
737 lation System over Southern South America: Sensitivity to Model Physics. *Weather and Forecasting*, 31
738 (1):217–236, February 2016. ISSN 0882-8156, 1520-0434. doi: 10.1175/WAF-D-14-00157.1.
- 739 María Eugenia Dillon, Paula Maldonado, Paola Corrales, Yanina García Skabar, Juan Ruiz, Maximiliano
740 Sacco, Federico Cutraro, Leonardo Mingari, Cynthia Matsudo, Luciano Vidal, Martin Rugna, María Paula
741 Hobouchian, Paola Salio, Stephen Nesbitt, Celeste Saulo, Eugenia Kalnay, and Takemasa Miyoshi. A
742 rapid refresh ensemble based data assimilation and forecast system for the RELAMPAGO field campaign.
743 *Atmospheric Research*, page 105858, September 2021. ISSN 0169-8095. doi: 10.1016/j.atmosres.2021.
744 105858.
- 745 Matt Dowle and Arun Srinivasan. Data.table: Extension of 'data.frame', July 2020.
- 746 J. R. Eyre, S. J. English, and M. Forsythe. Assimilation of satellite data in numerical weather prediction.
747 Part I: The early years. *Quarterly Journal of the Royal Meteorological Society*, 146(726):49–68, 2020.
748 ISSN 1477-870X. doi: 10.1002/qj.3654.
- 749 Fernando Garcia, Juan Ruiz, Paola Salio, Hernan Bechis, and Steve Nesbitt. Argentina mesonet data.
750 Version 1.1. UCAR/NCAR - earth observing laboratory., 2019.
- 751 Nicholas A. Gasperoni, Xuguang Wang, Keith A. Brewster, and Frederick H. Carr. Assessing Impacts of the
752 High-Frequency Assimilation of Surface Observations for the Forecast of Convection Initiation on 3 April
753 2014 within the Dallas–Fort Worth Test Bed. *Monthly Weather Review*, 146(11):3845–3872, November
754 2018. ISSN 1520-0493, 0027-0644. doi: 10.1175/MWR-D-18-0177.1.
- 755 Luis G. Goncalves de Goncalves, Luiz Sapucci, Eder Vendrasco, João Gerd de Mattos, Camila Ferreira,
756 Eduardo Khamis, and Nicolas Cruz. A rapid update data assimilation cycle over South America us-
757 ing 3DVar and EnKF. In *The 20th International TOVS Study Conference (ITSC-20)*, Lake Geneva,
758 Wisconsin, USA, 2015. The 20th International TOVS Study Conference (ITSC-20).
- 759 G. A. Grell and S. R. Freitas. A scale and aerosol aware stochastic convective parameterization for weather

- 760 and air quality modeling. *Atmospheric Chemistry and Physics Discussions*, 13(9):23845–23893, September
761 2013. ISSN 1680-7375. doi: 10.5194/acpd-13-23845-2013.
- 762 Nils Gustafsson, Tijana Janjić, Christoph Schraff, Daniel Leuenberger, Martin Weissmann, Hendrik Reich,
763 Pierre Brousseau, Thibaut Montmerle, Eric Wattrelot, Antonín Bučánek, Máté Mile, Rafiq Hamdi, Mag-
764 nus Lindskog, Jan Barkmeijer, Mats Dahlbom, Bruce Macpherson, Sue Ballard, Gordon Inverarity, Jacob
765 Carley, Curtis Alexander, David Dowell, Shun Liu, Yasutaka Ikuta, and Tadashi Fujita. Survey of data
766 assimilation methods for convective-scale numerical weather prediction at operational centres. *Quarterly*
767 *Journal of the Royal Meteorological Society*, 144(713):1218–1256, April 2018. ISSN 0035-9009, 1477-870X.
768 doi: 10.1002/qj.3179.
- 769 So-Young Ha and Chris Snyder. Influence of Surface Observations in Mesoscale Data Assimilation Using
770 an Ensemble Kalman Filter. *Monthly Weather Review*, 142(4):1489–1508, April 2014. ISSN 0027-0644,
771 1520-0493. doi: 10.1175/MWR-D-13-00108.1.
- 772 Y Han, Paul Van Delst, Q Liu, F. Weng, B. Yan, Russ Treadon, and John Derber. JCSDA Community
773 Radiative Transfer Model (CRTM)—version 1. Technical report, Washington, D.C., 2006.
- 774 H. Hersbach, B. Bell, P. Berrisford, G. Biavati, A. Horányi, J. Muñoz Sabater, J. Nicolas, C. Peubey,
775 R. Radu, I. Rozum, D. Schepers, A. Simmons, C. Soci, D. Dee, and J-N. Thépaut. ERA5 hourly data
776 on pressure levels from 1959 to present. *Copernicus Climate Change Service (C3S) Climate Data Store*
777 (*CDS*), (Accessed on <08-08-2022>), 2018. doi: 10.24381/cds.bd0915c6.
- 778 Song-You Hong, Ju-Hye Kim, Jeong-ock Lim, and Jimy Dudhia. The WRF Single Moment 6-Class Micro-
779 physics Scheme (WSM6). *Journal of the Korean Meteorological Society*, 42:129–151, March 2006a.
- 780 Song-You Hong, Yign Noh, and Jimy Dudhia. A New Vertical Diffusion Package with an Explicit Treatment
781 of Entrainment Processes. *Monthly Weather Review*, 134(9):2318–2341, September 2006b. ISSN 0027-
782 0644, 1520-0493. doi: 10.1175/MWR3199.1.
- 783 Ming Hu, Guoqing Ge, Chunhua Zhou, Don Stark, Hui Shao, Kathryn Newman, Jeff Beck, and Xin Zhang.
784 Grid-point Statistical Interpolation (GSI) User's Guide Version 3.7. Technical report, Developmental
785 Testbed Center, 2018.
- 786 George Huffman, David Bolvin, Dan Braithwaite, Kuolin Hsu, Robert Joyce, Christopher Kidd, Eric Nelkin,
787 S. Sorooshian, J. Tan, and Pingping Xie. NASA Global Precipitation Measurement (GPM) Integrated
788 Multi-satellitE Retrievals for GPM (IMERG). Technical report, National Aeronautics and Space Admin-
789 istration (NASA), February 2018.
- 790 Brian R. Hunt, Eric J. Kostelich, and Istvan Szunyogh. Efficient data assimilation for spatiotemporal chaos:
791 A local ensemble transform Kalman filter. *Physica D: Nonlinear Phenomena*, 230(1-2):112–126, June
792 2007. ISSN 01672789. doi: 10.1016/j.physd.2006.11.008.
- 793 Michael J. Iacono, Jennifer S. Delamere, Eli J. Mlawer, Mark W. Shephard, Shepard A. Clough, and

- 794 William D. Collins. Radiative forcing by long-lived greenhouse gases: Calculations with the AER radiative
795 transfer models. *Journal of Geophysical Research*, 113(D13):D13103, July 2008. ISSN 0148-0227. doi:
796 10.1029/2008JD009944.
- 797 Zaviša I. Janjić. The Step-Mountain Eta Coordinate Model: Further Developments of the Convection,
798 Viscous Sublayer, and Turbulence Closure Schemes. *Monthly Weather Review*, 122(5):927–945, May
799 1994. ISSN 0027-0644. doi: 10.1175/1520-0493(1994)122<0927:TSMECM>2.0.CO;2.
- 800 Thomas A. Jones, Jason A. Otkin, David J. Stensrud, and Kent Knopfmeier. Assimilation of Satellite
801 Infrared Radiances and Doppler Radar Observations during a Cool Season Observing System Simulation
802 Experiment. *Monthly Weather Review*, 141(10):3273–3299, October 2013. ISSN 0027-0644, 1520-0493.
803 doi: 10.1175/MWR-D-12-00267.1.
- 804 John S Kain. The Kain-Fritsch Convective Parameterization: An Update. *JOURNAL OF APPLIED
805 METEOROLOGY*, 43:12, 2004.
- 806 Xin-Zhong Liang, Qi Li, Haixia Mei, and Mingjian Zeng. Multi-Grid Nesting Ability to Represent Convec-
807 tions Across the Gray Zone. *Journal of Advances in Modeling Earth Systems*, 11(12):4352–4376, 2019.
808 ISSN 1942-2466. doi: 10.1029/2019MS001741.
- 809 Agnes H. Lim, James A. Jung, Hung-Lung A. Huang, Steven A. Ackerman, and Jason A. Otkin. Assimilation
810 of clear sky Atmospheric Infrared Sounder radiances in short-term regional forecasts using community
811 models. *Journal of Applied Remote Sensing*, 8(1):083655, April 2014. ISSN 1931-3195, 1931-3195. doi:
812 10.1117/1.JRS.8.083655.
- 813 Haidao Lin, Stephen S. Weygandt, Stanley G. Benjamin, and Ming Hu. Satellite Radiance Data Assimilation
814 within the Hourly Updated Rapid Refresh. *Weather and Forecasting*, 32(4):1273–1287, August 2017. ISSN
815 0882-8156. doi: 10.1175/WAF-D-16-0215.1.
- 816 Yasumitsu Maejima, Takemasa Miyoshi, Masaru Kunii, Hiromu Seko, and Kae Sato. Impact of Dense and
817 Frequent Surface Observations on 1-Minute-Update Severe Rainstorm Prediction: A Simulation Study.
818 *Journal of the Meteorological Society of Japan. Ser. II*, 97(1):253–273, 2019. doi: 10.2151/jmsj.2019-014.
- 819 Paula Maldonado, Juan Ruiz, and Celeste Saulo. Parameter Sensitivity of the WRF-LETKF Sys-
820 tem for Assimilation of Radar Observations: Imperfect-Model Observing System Simulation Experi-
821 ments. *Weather and Forecasting*, 35(4):1345–1362, August 2020. ISSN 1520-0434, 0882-8156. doi:
822 10.1175/WAF-D-19-0161.1.
- 823 Paula Maldonado, Juan Ruiz, and Celeste Saulo. Sensitivity to Initial and Boundary Perturbations in
824 Convective-Scale Ensemble-Based Data Assimilation: Imperfect-Model OSSEs. *SOLA*, 17(0):96–102,
825 2021. ISSN 1349-6476. doi: 10.2151/sola.2021-015.
- 826 Swapna Mallick and Thomas A. Jones. Assimilation of GOES-16 satellite derived winds into the warn-on-
827 forecast system. *Atmospheric Research*, 245:105131, November 2020. ISSN 0169-8095. doi: 10.1016/j.

- 828 atmosres.2020.105131.
- 829 Paul Markowski and Yvette Richardson. Organization of Isolated Convection. In *Mesoscale Meteorology in*
830 *Midlatitudes*, chapter 8, pages 201–244. John Wiley & Sons, Ltd, 2010. ISBN 978-0-470-68210-4. doi:
831 10.1002/9780470682104.ch8.
- 832 C. Matsudo, Yanina García Skabar, Juan Ruiz, Luciano Vidal, and Paola Salio. Verification of WRF-ARW
833 convective-resolving forecasts over Southeastern South America. *Mausam*, 66:445–456, July 2015.
- 834 Cynthia Matsudo, María Alejandra Salles, and Yanina García Skabar. Verificación de los pronósticos del
835 esquema determinístico del modelo WRF para el año 2020. July 2021.
- 836 Mikio Nakanishi and Hiroshi Niino. Development of an Improved Turbulence Closure Model for the At-
837 mospheric Boundary Layer. *Journal of the Meteorological Society of Japan*, 87(5):895–912, 2009. ISSN
838 0026-1165. doi: 10.2151/jmsj.87.895.
- 839 National Centers for Environmental Prediction, National Weather Service, NOAA, U.S. Department of
840 Commerce. NCEP GFS 0.25 degree global forecast grids historical archive. 2015.
- 841 Tobias Necker, Stefan Geiss, Martin Weissmann, Juan Ruiz, Takemasa Miyoshi, and Guo-Yuan Lien. A
842 convective-scale 1,000-member ensemble simulation and potential applications. *Quarterly Journal of*
843 *the Royal Meteorological Society*, 146(728):1423–1442, April 2020. ISSN 0035-9009, 1477-870X. doi:
844 10.1002/qj.3744.
- 845 Stephen W. Nesbitt, Paola V. Salio, Eldo Ávila, Phillip Bitzer, Lawrence Carey, V. Chandrasekar, Wiebke
846 Deierling, Francina Dominguez, Maria Eugenia Dillon, C. Marcelo Garcia, David Gochis, Steven Good-
847 man, Deanna A. Hence, Karen A. Kosiba, Matthew R. Kumjian, Timothy Lang, Lorena Medina Luna,
848 James Marquis, Robert Marshall, Lynn A. McMurdie, Ernani Lima Nascimento, Kristen L. Rasmussen,
849 Rita Roberts, Angela K. Rowe, Juan José Ruiz, Eliah F. M. T. São Sabbas, A. Celeste Saulo, Russ S. Schu-
850 macher, Yanina García Skabar, Luiz Augusto Toledo Machado, Robert J. Trapp, Adam Varble, James
851 Wilson, Joshua Wurman, Edward J. Zipser, Ivan Arias, Hernán Bechis, and Maxwell A. Grover. A storm
852 safari in Subtropical South America: Proyecto RELAMPAGO. *Bulletin of the American Meteorological*
853 *Society*, -1(aop):1–64, April 2021. ISSN 0003-0007, 1520-0477. doi: 10.1175/BAMS-D-20-0029.1.
- 854 Michiko Otsuka, Masaru Kunii, Hiromu Seko, Kazuki Shimoji, Masahiro Hayashi, and Koji Yamashita.
855 Assimilation Experiments of MTSAT Rapid Scan Atmospheric Motion Vectors on a Heavy Rainfall Event.
856 *Journal of the Meteorological Society of Japan. Ser. II*, 93(4):459–475, 2015. doi: 10.2151/jmsj.2015-030.
- 857 Rachida El Ouaraini, Loïk Berre, Claude Fischer, and El Hassan Sayouty. Sensitivity of regional ensemble
858 data assimilation spread to perturbations of lateral boundary conditions. *Tellus A: Dynamic Meteorology*
859 *and Oceanography*, 67(1):28502, December 2015. ISSN null. doi: 10.3402/tellusa.v67.28502.
- 860 R Core Team. *R: A Language and Environment for Statistical Computing*. R Foundation for Statistical
861 Computing, Vienna, Austria, 2020.

- 862 Kristen L. Rasmussen, Manuel D. Zuluaga, and Robert A. Houze. Severe convection and lightning in
863 subtropical South America. *Geophysical Research Letters*, 41(20):7359–7366, 2014. ISSN 1944-8007. doi:
864 10.1002/2014GL061767.
- 865 Brett Roberts, Burkely T. Gallo, Israel L. Jirak, Adam J. Clark, David C. Dowell, Xuguang Wang, and
866 Yongming Wang. What Does a Convection-Allowing Ensemble of Opportunity Buy Us in Forecasting
867 Thunderstorms? *Weather and Forecasting*, 35(6):2293–2316, December 2020. ISSN 0882-8156, 1520-0434.
868 doi: 10.1175/WAF-D-20-0069.1.
- 869 Nigel Roberts. Assessing the spatial and temporal variation in the skill of precipitation forecasts from an
870 NWP model. *Meteorological Applications*, 15(1):163–169, 2008. ISSN 1469-8080. doi: 10.1002/met.57.
- 871 Juan J. Ruiz, Celeste Saulo, and Julia Nogués-Paegle. WRF Model Sensitivity to Choice of Parameterization
872 over South America: Validation against Surface Variables. *Monthly Weather Review*, 138(8):3342–3355,
873 August 2010. ISSN 0027-0644. doi: 10.1175/2010MWR3358.1.
- 874 Masahiro Sawada, Zaizhong Ma, Avichal Mehra, Vijay Tallapragada, Ryo Oyama, and Kazuki Shimoji. Im-
875 pacts of Assimilating High-Resolution Atmospheric Motion Vectors Derived from Himawari-8 on Tropical
876 Cyclone Forecast in HWRF. *Monthly Weather Review*, 147(10):3721–3740, October 2019. ISSN 1520-0493,
877 0027-0644. doi: 10.1175/MWR-D-18-0261.1.
- 878 Hui Shao, John Derber, Xiang-Yu Huang, Ming Hu, Kathryn Newman, Donald Stark, Michael Lueken,
879 Chunhua Zhou, Louisa Nance, Ying-Hwa Kuo, and Barbara Brown. Bridging Research to Operations
880 Transitions: Status and Plans of Community GSI. *Bulletin of the American Meteorological Society*, 97
881 (8):1427–1440, August 2016. ISSN 0003-0007, 1520-0477. doi: 10.1175/BAMS-D-13-00245.1.
- 882 Randhir Singh, Satya P. Ojha, C. M. Kishtawal, P. K. Pal, and A. S. Kiran Kumar. Impact of the assimilation
883 of INSAT-3D radiances on short-range weather forecasts: Assimilation of INSAT-3D Radiances. *Quarterly
884 Journal of the Royal Meteorological Society*, 142(694):120–131, January 2016. ISSN 00359009. doi:
885 10.1002/qj.2636.
- 886 William C Skamarock, Joseph B Klemp, Jimy Dudhia, David O Gill, Dale M Barker, Michael G Duda,
887 Xiang-Yu Huang, Wei Wang, and Jordan G Powers. A Description of the Advanced Research WRF
888 Version 3. Technical report, June 2008.
- 889 Juanzhen Sun, Ming Xue, James W. Wilson, Ishtar Zawadzki, Sue P. Ballard, Jeanette Onvlee-Hooimeyer,
890 Paul Joe, Dale M. Barker, Ping-Wah Li, Brian Golding, Mei Xu, and James Pinto. Use of NWP for Now-
891 casting Convective Precipitation: Recent Progress and Challenges. *Bulletin of the American Meteorolog-
892 ical Society*, 95(3):409–426, March 2014. ISSN 0003-0007, 1520-0477. doi: 10.1175/BAMS-D-11-00263.1.
- 893 UCAR/NCAR - Earth Observing Laboratory. Multi-network composite highest resolution radiosonde data.
894 Version 1.3. UCAR/NCAR - earth observing laboratory., 2020.
- 895 Zheng Qi Wang and Roger Randriamampianina. The Impact of Assimilating Satellite Radiance Observations

- 896 in the Copernicus European Regional Reanalysis (CERRA). *Remote Sensing*, 13(3):426, January 2021.
897 ISSN 2072-4292. doi: 10.3390/rs13030426.
- 898 Peter Weston, Alan Geer, Niels Bormann, and Niels Bormann. Investigations into the assimilation of
899 AMSU-A in the presence of cloud and precipitation, 2019. ISSN 50.
- 900 DUSTAN M. WHEATLEY and DAVID J. STENSrud. The Impact of Assimilating Surface Pressure Observations
901 on Severe Weather Events in a WRF Mesoscale Ensemble System. *Monthly Weather Review*, 138(5):
902 1673–1694, May 2010. ISSN 1520-0493, 0027-0644. doi: 10.1175/2009MWR3042.1.
- 903 Jeffrey S. Whitaker and Thomas M. Hamill. Evaluating Methods to Account for System Errors in Ensemble
904 Data Assimilation. *Monthly Weather Review*, 140(9):3078–3089, September 2012. ISSN 0027-0644, 1520-
905 0493. doi: 10.1175/MWR-D-11-00276.1.
- 906 Hadley Wickham. *Ggplot2: Elegant Graphics for Data Analysis*. Use R! Springer-Verlag, New York, 2009.
907 ISBN 978-0-387-98141-3. doi: 10.1007/978-0-387-98141-3.
- 908 Ting-Chi Wu, Hui Liu, Sharanya J. Majumdar, Christopher S. Velden, and Jeffrey L. Anderson. Influence
909 of Assimilating Satellite-Derived Atmospheric Motion Vector Observations on Numerical Analyses and
910 Forecasts of Tropical Cyclone Track and Intensity. *Monthly Weather Review*, 142(1):49–71, January 2014.
911 ISSN 1520-0493, 0027-0644. doi: 10.1175/MWR-D-13-00023.1.
- 912 Yihui Xie. *Dynamic Documents with R and Knitr*. Chapman and Hall/CRC, Boca Raton, Florida, second
913 edition, 2015.
- 914 J. Zhao, Jidong Gao, Thomas A. Jones, and Junjun Hu. Impact of Assimilating High-Resolution Atmospheric
915 Motion Vectors on Convective Scale Short-Term Forecasts: 1. Observing System Simulation Experiment
916 (OSSE). *Journal of Advances in Modeling Earth Systems*, 13(10):e2021MS002484, 2021a. ISSN 1942-2466.
917 doi: 10.1029/2021MS002484.
- 918 J. Zhao, Jidong Gao, Thomas A. Jones, and Junjun Hu. Impact of Assimilating High-Resolution Atmospheric
919 Motion Vectors on Convective Scale Short-Term Forecasts: 2. Assimilation Experiments of GOES-16
920 Satellite Derived Winds. *Journal of Advances in Modeling Earth Systems*, 13(10):e2021MS002486, 2021b.
921 ISSN 1942-2466. doi: 10.1029/2021MS002486.
- 922 Kefeng Zhu, Ming Xue, Yujie Pan, Ming Hu, Stanley G. Benjamin, Stephen S. Weygandt, and Haidao
923 Lin. The Impact of Satellite Radiance Data Assimilation within a Frequently Updated Regional Forecast
924 System Using a GSI-based Ensemble Kalman Filter. *Advances in Atmospheric Sciences*, 36(12):1308–
925 1326, December 2019. ISSN 0256-1530, 1861-9533. doi: 10.1007/s00376-019-9011-3.
- 926 Yanqiu Zhu, John Derber, Andrew Collard, Dick Dee, Russ Treadon, George Gayno, and James A. Jung.
927 Enhanced radiance bias correction in the National Centers for Environmental Prediction’s Gridpoint
928 Statistical Interpolation data assimilation system. *Quarterly Journal of the Royal Meteorological Society*,
929 140(682):1479–1492, 2014. ISSN 1477-870X. doi: 10.1002/qj.2233.

930 Yanqiu Zhu, Emily Liu, Rahul Mahajan, Catherine Thomas, David Groff, Paul Van Delst, Andrew Collard,
931 Daryl Kleist, Russ Treadon, and John C. Derber. All-Sky Microwave Radiance Assimilation in NCEP's
932 GSI Analysis System. *Monthly Weather Review*, 144(12):4709–4735, September 2016. ISSN 0027-0644.
933 doi: 10.1175/MWR-D-15-0445.1.

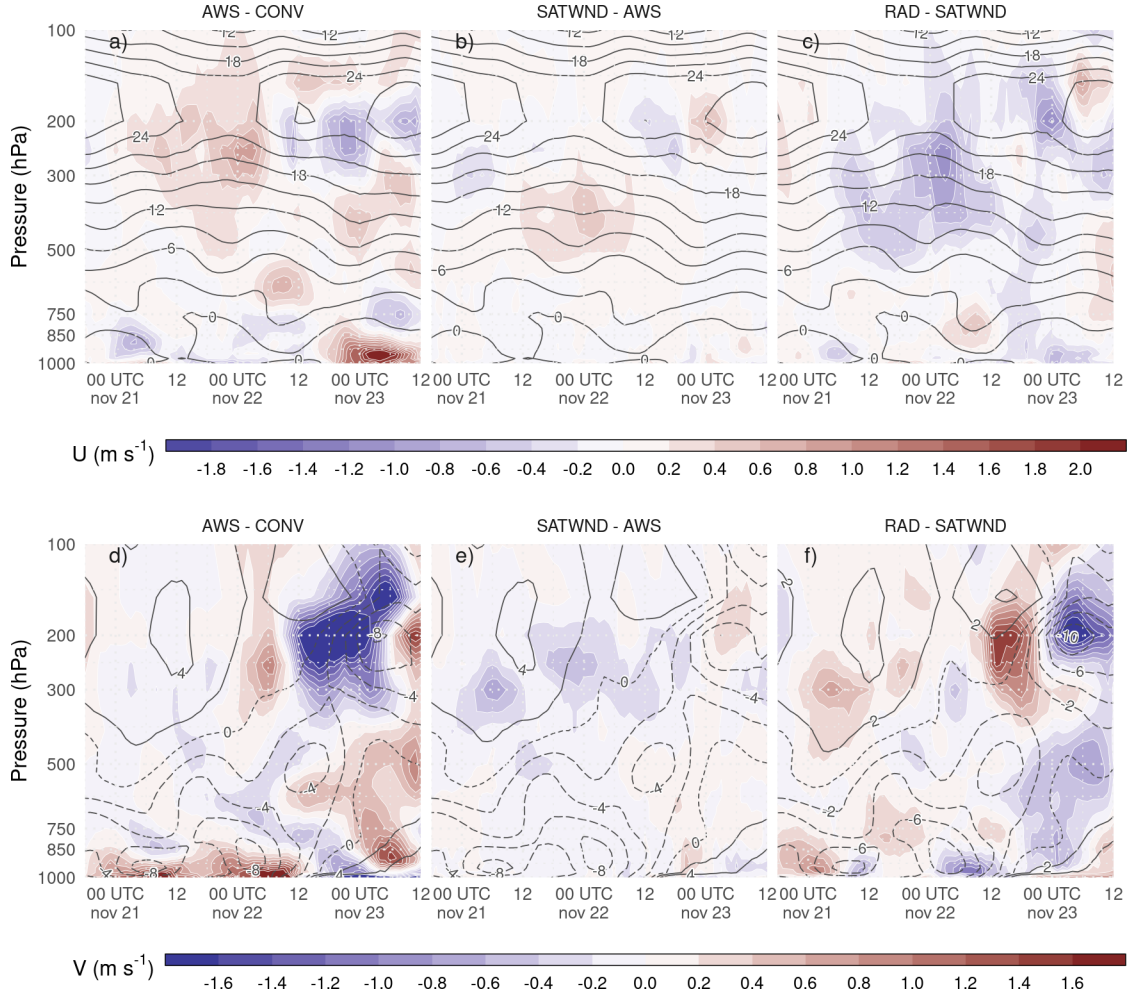


Figure 9: Difference between analysis ensemble mean experiments a) and d) AWS-CONV, b) and e) SATWND-AWS, and c) and f) RAD-SATWND for the spatially averaged vertical profiles of u wind (a, b, and c, in $m s^{-1}$) and v wind (d, e, and f in $m s^{-1}$) calculated over the inner domain (red box in Figure 2a) for each analysis cycle. Black contours correspond to u wind and dashed contours to negative v wind for (a) AWS, (b) SATWND, and (c) RAD and v wind for (d) AWS, (e) SATWND, and (f) RAD since those experiments are the ones with more assimilated observations in each panel.

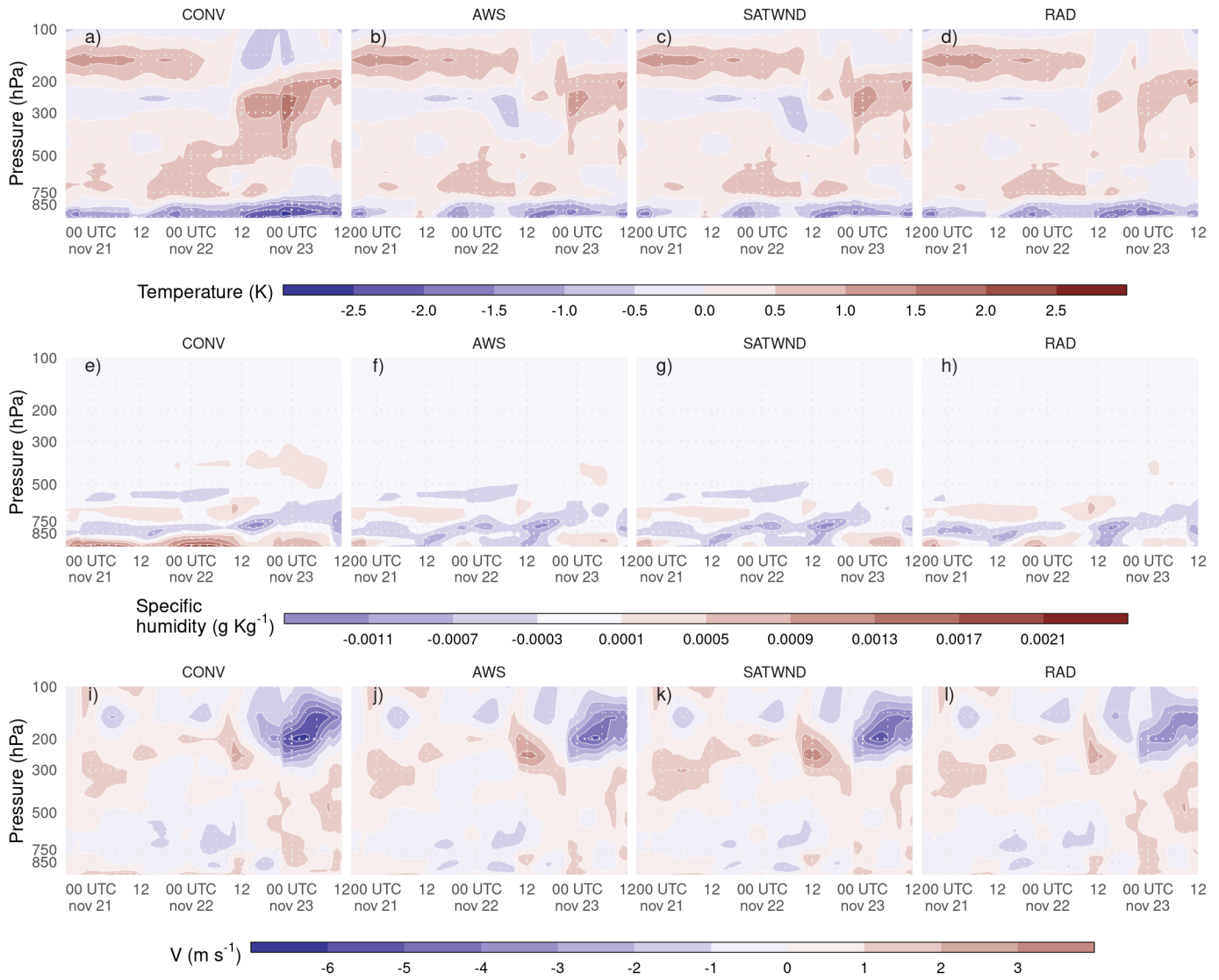


Figure 10: Difference between ERA5 and the analysis ensemble mean experiments for the spatially averaged vertical profiles of air temperature (K, a–d), specific humidity (g Kg^{-1} , e–h) and meridional wind (m s^{-1} , i–l) calculated over the inner domain (red box in Figure 2a) for each analysis cycle.

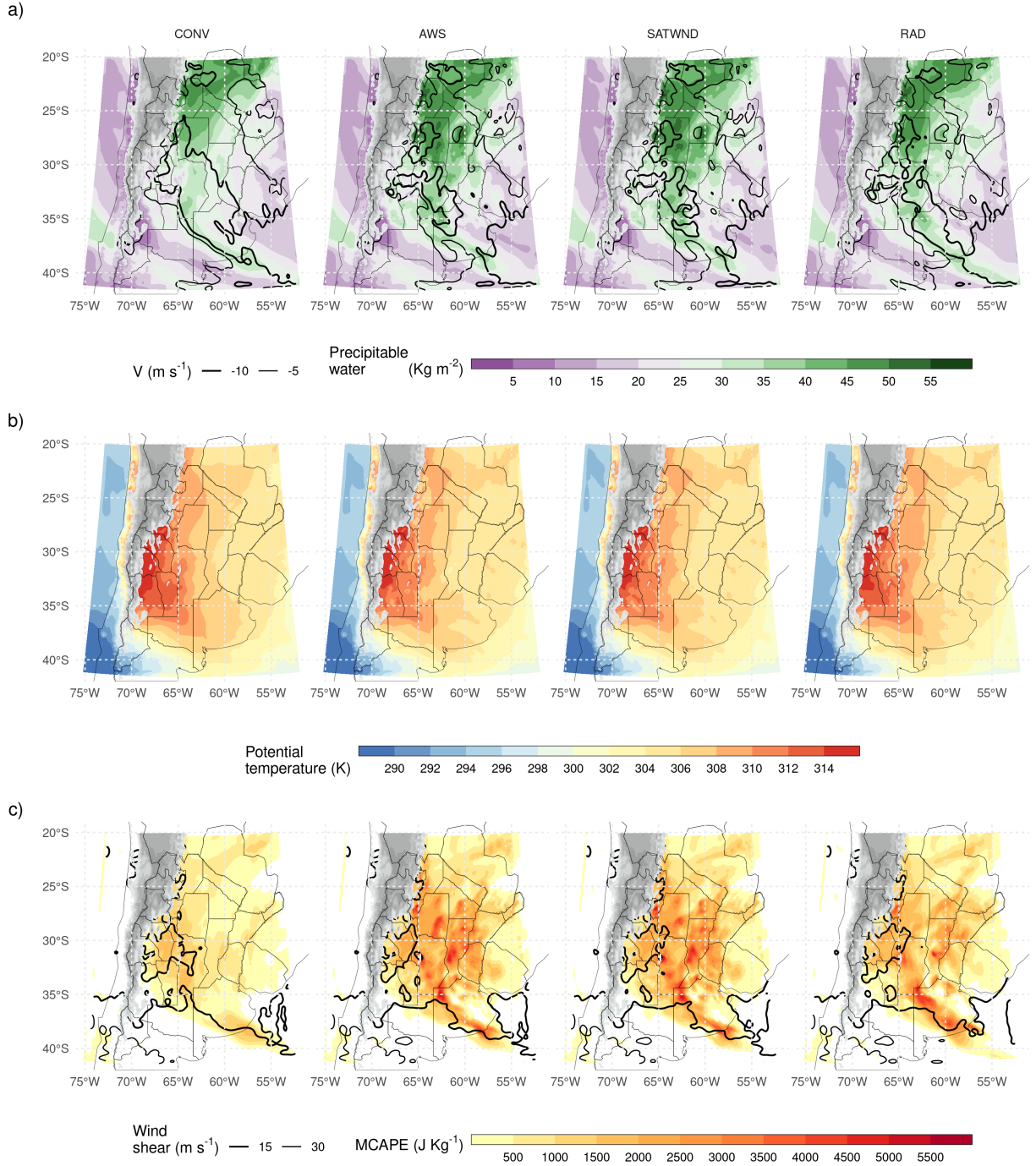


Figure 11: a) Precipitable water (shaded, kg m^{-2}) and average northerly wind over the first 7 sigma levels (from the surface up to approximately 800 hPa, contours, m s^{-1}), b) Average potential temperature for the PBL (first 10 sigma levels), and c) Maximum CAPE and \sim 0-6 km wind shear over 15 and 30 m s^{-1} for each experiment. All fields correspond to the analysis ensemble mean for 00 UTC Nov 22. Grey filled contours correspond to topography over 1500 meters above sea level.

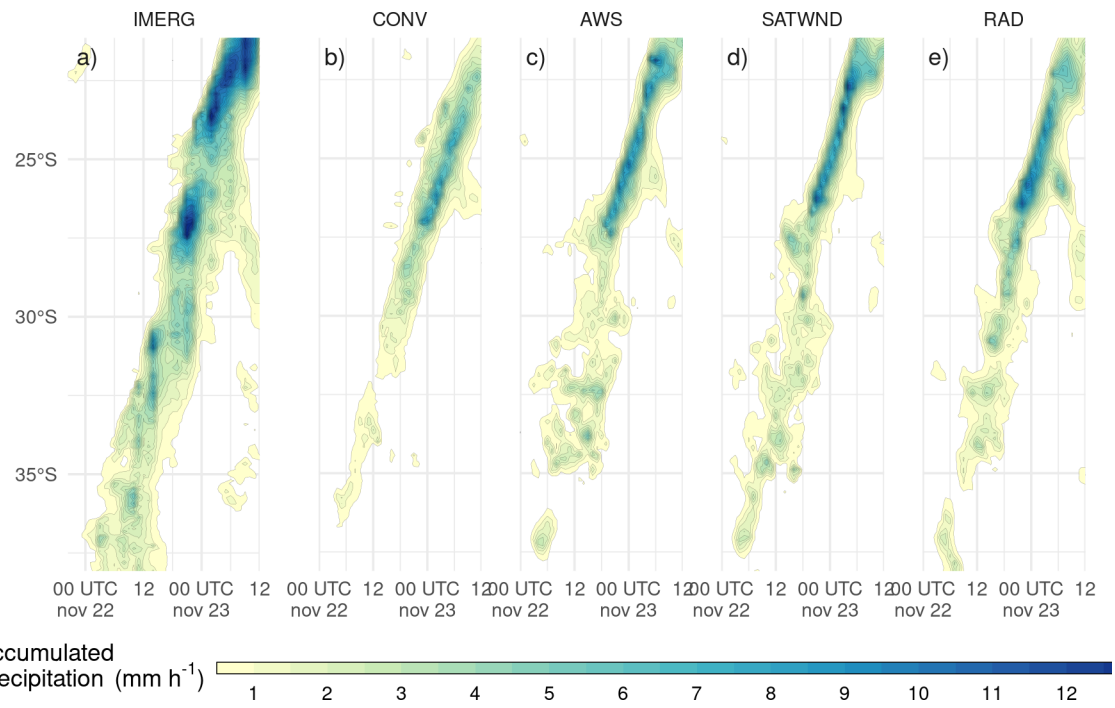


Figure 12: Hövmoller diagram of probability matched mean hourly accumulated 1-h forecast precipitation for each latitude band estimated by IMERG (left) and simulated (right), for the ensemble mean of each experiment, averaged over a longitude range between 67°W and 54.5°W . Contours drawn every 0.5 mm h^{-1} , starting at 0.5 mm h^{-1} .

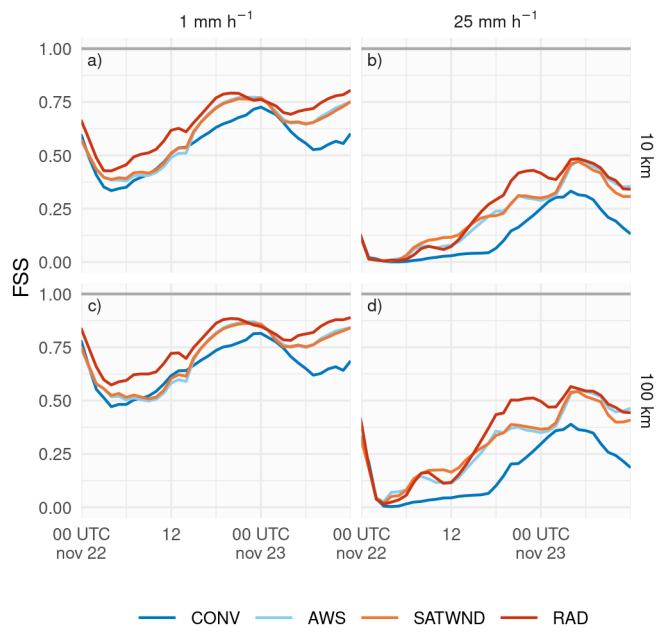


Figure 13: FSS calculated over 1-h forecast precipitation accumulated in a 6-hour moving window for 1 mm (a and c) and 25 mm (b and d) thresholds, on 10 km (a and b) and 100 km (c and d) scales, for the first-guess of CONV (blue line), AWS (light blue line), SATWND (orange line) and RAD (red line) experiments.

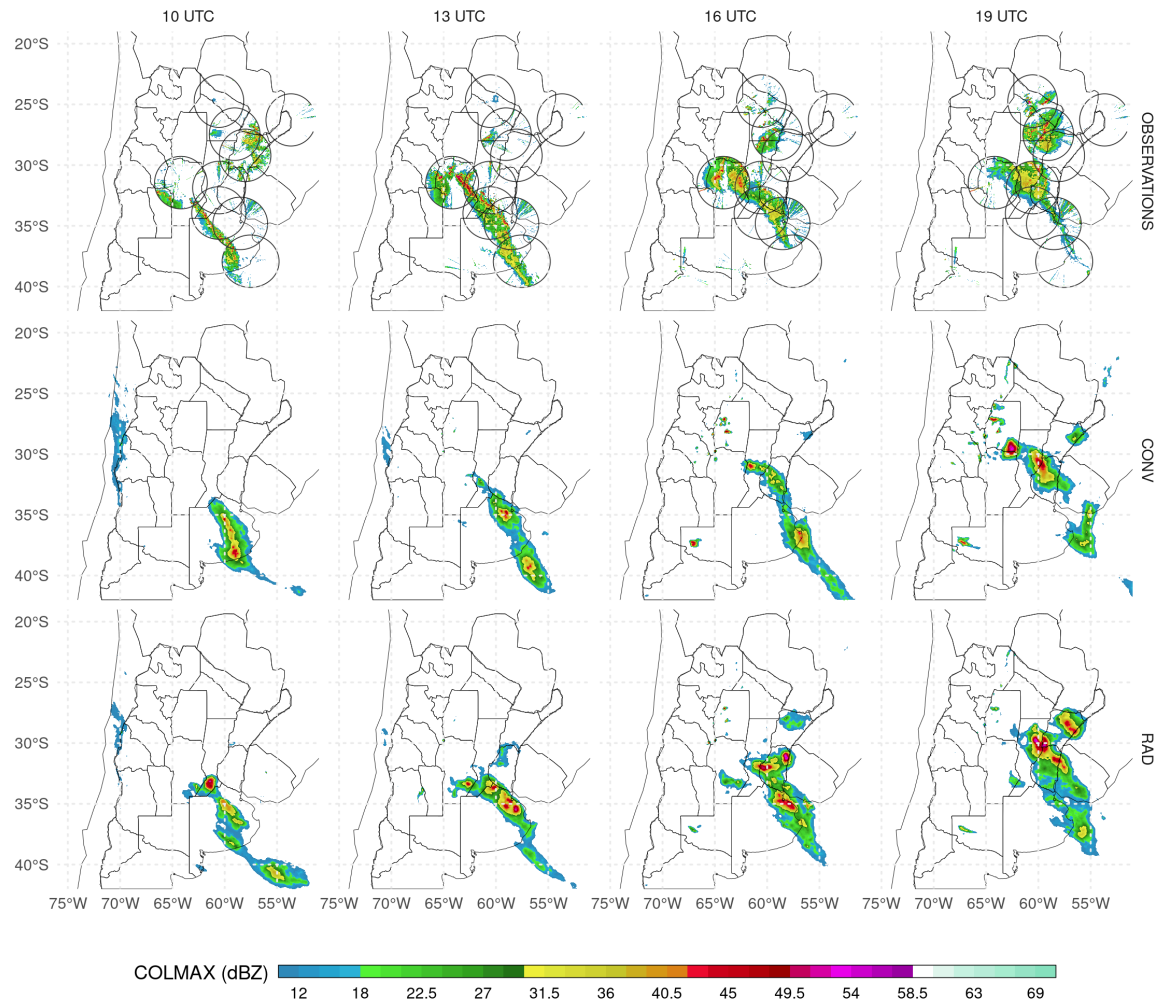


Figure 14: Maximum reflectivity in the column (COLMAX in dBZ), observed (upper row) and 1-hr forecast probability matched mean column maximum reflectivity for CONV (second row) and RAD (third row) at 10 UTC (first column), 13 UTC (second column), 16 UTC (third column), and 19 UTC (fourth column) Nov 22, 2018. Black circles in first row show the observation range of each radar.

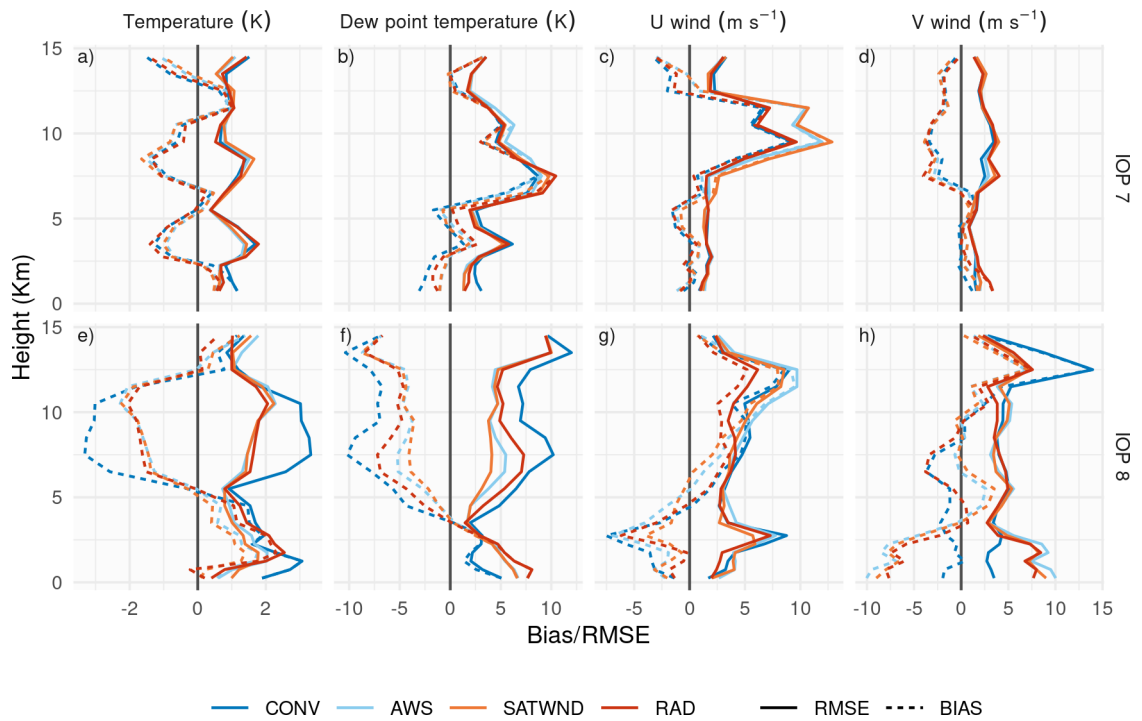


Figure 15: RMSE (solid line) and Bias (dashed line) of a) temperature (K), b) dew point temperature (K), c) u wind ($m s^{-1}$) and d) v wind ($m s^{-1}$) calculated by comparing the analysis of each experiment with the RELAMPAGO soundings during IOP 7 and IOP 8. The blue line corresponds to CONV, the light blue line to AWS, SATWND is represented with an orange line, and RAD with a red line.

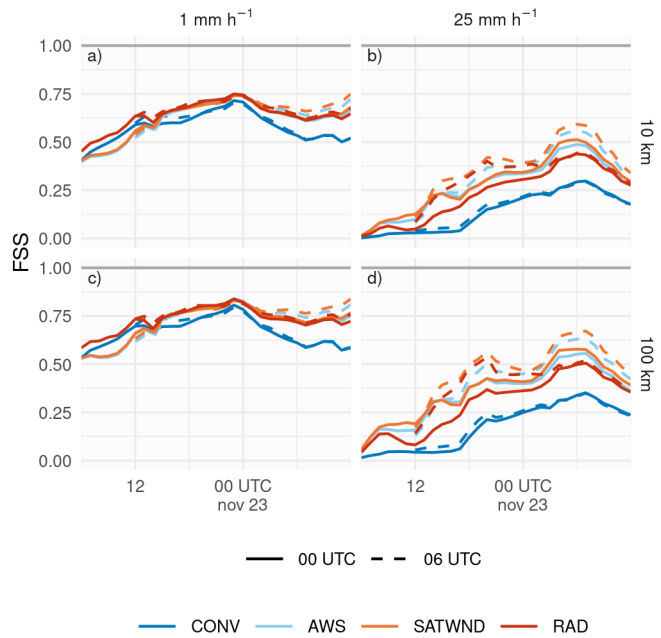


Figure 16: FSS calculated over a 6-hour moving window for 1 mm (a and c) and 25 mm (b and d) thresholds, on 10 km (a and b) and 100 km (c and d) scales, for the forecasts initialized from CONV (blue line), AWS (light blue line), SATWND (orange line), and RAD (red line) experiments at 00 UTC (solid line) and 06 UTC (dashed line), Nov 22.